DESIGN OF STREAMLINE-TRACED INLETS AND
THEIR INTEGRATION WITH ROTATING DETONATION ENGINES

by

MALCOLM LEE BRANCH

THESIS

Submitted in partial fulfillment of the requirements
for the degree of Master of Science in Aerospace Engineering at
The University of Texas at Arlington
August, 2021

Arlington, Texas

Supervising Committee:

Liwei Zhang, Co-Advisor
Frank Lu, Co-Advisor
Donald Wilson

Acknowledgements

With a deep sense of gratitude, I would like to thank my advisor Dr. Liwei Zhang and co-advisor Dr. Frank Lu for their guidance, expertise, and encouragement. I would like to thank Dr. Andrew Mizener for access to his engine codes and advice on the RDE engine performance. My thanks also goes out to my thesis committee: Dr. Liwei Zhang, Dr. Frank Lu, and Dr. Donald Wilson.

I am honored that I was allowed the opportunity to conduct research at the Computational Aerothermodynamics Lab. I am grateful for those at CAL for their support, encouragement, and listening ear.

<div align="right">July 02, 2021</div>

Abstract

DESIGN OF STREAMLINE-TRACED INLETS AND
THEIR INTEGRATION WITH ROTATING DETONATION ENGINES

Malcolm Lee Branch

The University of Texas at Arlington, 2021

Supervising Professors: Liwei Zhang & Frank K. Lu

This thesis has two parts: 1) design of the streamline-traced inlets (STIs); and 2) integration of STIs with rotating detonation engines (RDEs). The STI design starts with a two-dimensional, isentropic compression flowfield as the parent flowfield. The method of characteristics was used to generate the flowfield throughout the entire STI. For a given flight altitude 18 km, freestream Mach number $M_\infty = 3.0$, and inlet exit-plane Mach number $M_\omega = 1.2$, a parametric sweep of the initial deflection angle $\theta_1 = 4.0$–11.0 deg and the Mach number at the entrance of the internal compression system $M_3 = 1.3$–1.7 was performed to determine the STI performance sensitivity as a function of the design parameters. By using a variant of gradient-descent optimization, the optimal STI was chosen for the greatest combination of total pressure recovery and volumetric efficiency. By changing the type of internal compression system, two STIs were designed: STI–1 used a single-sided internal compression system, and STI–2 used a symmetrical internal compression system. At the design Mach number, it was found that STI–2 exhibited better performance than STI–1. The total pressure recovery of STI–2 was approximately five percent higher than that in STI–1. For volumetric efficiency, the difference between the STIs was marginal where STI–2 exceeded STI–1 by less than one percent.

For the off-design cases, the commercial computational fluid dynamic package ANSYS Fluent was used to simulate the flowfields. The freestream Mach number was varied from 2.9 to 3.4. The freestream Mach number was limited to 3.4 due to the auto-ignition temperature of the RDE fuels. It was assumed that if the total temperature of the flow entering the RDE

exceeded the minimum of the auto-ignition temperature range, the fuel would auto-ignite and not detonate as intended. For the range of freestream Mach number, the local Mach number and static pressure were determined at the inlet exit plane. In general, the total pressure recovery of both STIs exceeded the minimum established by MIL-E-5007D with exception of the subcritical speeds where both fell below the minimum. The total pressure recovery of STI–2 exceeded that of STI–1 throughout the entire range of Mach numbers.

In the second part of the thesis, the integration of STI and RDE was explored. First, a parametric sweep was performed to select an RDE annulus configuration with the total pressure and total temperature obtained from the STI design. For both fuels considered, propane and hydrogen, the parametric sweep varied the engine annulus length $l = 15.0$–50.0 cm to determine the RDE performance sensitivity as a function of design parameters. The RDEs were evaluated for their performance in regard to thrust, resultant torque, fuel-based specific impulse, and thrust-specific fuel consumption. A RDE annulus with a short length and wide thickness was chosen for both STIs using hydrogen as fuel. Second, the performance of the integrated STI/RDE systems were assessed. Internal ducting, including inlet isolator, was neglected; therefore, the total pressure value at the STI exit plane was used as the total pressure at the entrance of the RDE. For the chosen RDE annulus, over the entire range of Mach numbers, the RDE exhibited a slightly greater thrust for propane over hydrogen, and a slightly greater thrust for STI–2 than STI–1. For the resultant torque, hydrogen yielded a greater value than propane, and the RDE integrated with STI–2 exhibited a slightly greater torque than the system integrated with STI–1. For the fuel-based specific impulse, the cases with hydrogen were found to be approximately 2.3 times greater than the cases using propane. For the thrust-specific fuel consumption, the cases with propane were found to be approximately 2.4 times greater than the cases with hydrogen. There was no significant difference in the fuel-based specific impulse and thrust-specific fuel consumption for both STI designs. Within the context of this study, optimal performance was found for the STI–2 design utilizing hydrogen as the fuel.

Table of Contents

List of Figures

List of Tables

Nomenclature

A = area, m^2

a = speed of sound, m/s

$C_\pm$ = left-running C_+ or right-running C_- characteristic lines

c_p = specific heat at constant pressure, J/(kg $\cdot$ K)

d_i = inner diameter of RDE annulus, cm

d_o = outer diameter of RDE annulus, cm

e = specific internal energy, J/kg

F = total resultant force, N

g_0 = gravitational acceleration at sea level, 9.81 m/s^2

h = specific enthalpy, J/kg

I_{sp} = specific impulse, s

$K_\pm$ = compatibility constant of a left-running K_+ or right-running K_- characteristic line

l = length, m

M = Mach number

M_ω = inlet terminal Mach number

$\dot{m}_f$ = fuel mass flow rate, kg/s

$\dot{m}_{inj}$ = propellant (fuel and oxidizer) mass flow rate, kg/s

p = static pressure, Pa

q = dynamic pressure, Pa

R = specific gas constant, J/(kg $\cdot$ K)

r_m = mean annular radius, cm

s = contour length of a single segment of the inlet body or cowl, m

s_w = wetted surface area, m^2

T = static temperature, K

$\mathbf{u}$ = velocity vector, m/s

$u,\ v$ = velocity components in the x- and y-directions, m/s

V $\quad=\quad$ velocity magnitude, m/s

$\mathbb{V}$ $\quad=\quad$ volume, m^3

w $\quad=\quad$ inlet width, m

$x,\ y$ $\quad=\quad$ Cartesian coordinates, m

y_c $\quad=\quad$ inlet capture height, m

β $\quad=\quad$ oblique shock angle, deg

γ $\quad=\quad$ ratio of specific heats

δ_a $\quad=\quad$ annulus thickness, cm

$\eta_{\mathbb{V}}$ $\quad=\quad$ volumetric efficiency

θ $\quad=\quad$ deflection or flow angle, deg

θ_1 $\quad=\quad$ inlet initial deflection angle, deg

λ $\quad=\quad$ characteristic slope

Λ $\quad=\quad$ detonation wave height, cm

μ $\quad=\quad$ Mach wave angle, deg

ν $\quad=\quad$ Prandtl–Meyer angle, deg

π $\quad=\quad$ total pressure recovery

ρ $\quad=\quad$ density, kg/m^3

τ $\quad=\quad$ torque, N $\cdot$ m

Subscripts:

body $\quad=\quad$ inlet body

cowl $\quad=\quad$ inlet cowl

i, j $\quad=\quad$ upstream and downstream of a shock, indexes of differing sizes

in $\quad=\quad$ RDE control volume injection plane

int $\quad=\quad$ beginning of the internal compression system

isen $\quad=\quad$ isentropic region of the inlet

n $\quad=\quad$ normal to the shock

out	$=$	RDE control volume exit plane
t	$=$	total or stagnation value
z	$=$	axial direction
θ	$=$	circumferential direction
ω	$=$	inlet exit
∞	$=$	freestream
1	$=$	uniform flow region upstream of the isentropic compression region
2	$=$	uniform flow region downstream of the isentropic compression region
3	$=$	flow region located at the entrance to the internal compression system
4	$=$	flow region located upstream of the terminal normal shock of the inlet

1 Introduction and Background

In recent years, much attention has been aimed at achieving airbreathing, hypersonic propulsion. A primary objective in working toward this goal has been designing highly-integrated airframe/propulsion systems. This integration results in highly coupled component systems. Such studies have largely been performed for scramjet engines [1, 2]. These integrated designs are typically applied to a waverider airframe [3–6]. The flow is compressed by the waverider forebody before entering an internal duct and combustor. In addition to compressing the flow, the forebody must consider the performance of the entire vehicle. To this end, the forebody is required to have good aerodynamic and volumetric properties. Various inlet geometries have been considered for similar applications over a range of flight conditions [3, 7–10].

For the present study, the forebody geometry considered is a streamline-traced inlet (STI). This geometry was chosen for its particular method of compressing the flow. Throughout the STI design process, the geometry was considered in regard to the aerodynamic and volumetric performance. These considerations are related to combustion unit performance and the volumetric performance of the entire vehicle, respectively.

In this work, the STI is coupled with a rotating detonation engine (RDE). In an RDE, a detonation wave continuously propagates circumferentially around an annulus with the high-pressure combustion products expelled rearward through a nozzle, thereby generating thrust. Introduced in the late 1950s, RDEs have been gaining interest in recent years due to geometry and operational simplicity amongst various advantages [11–13]. The RDE in the present study is sized to result in the best operating performance for the integrated STI/RDE system.

1

1.1   Streamline-Traced Inlet

Supersonic inlets are required to capture the correct amount of flow, compress and diffuse it to subsonic speeds at the engine face. A terminal shock is commonly used in the final phase of the supersonic inlet to decelerate the flow to subsonic speeds [14]. In the past, the majority of supersonic aircraft inlets have been pitot, two-dimensional or axisymmetric spike. The pitot inlet utilizes a terminal normal shock to slow the flow to subsonic speeds. An example of a pitot inlet can be seen on the Lockheed Martin F-16 [7]. The two-dimensional inlet utilizes a number of deflection ramps to create an oblique shock system before terminating with a normal shock. An example of a two-dimensional inlet can be seen on the McDonnell Douglas F-15 [8]. An axisymmetric spike inlet utilizes a conical spike centerbody to decelerate the flow through a conical shock system. An example of an axisymmetric spike inlet can be seen on the Convair B-58 [9].

Minimizing the number and/or strength of shock waves present in the inlet can lead to maximizing the total pressure recovery of the inlet. One technique to minimize the number of shocks in the inlet is to make use of streamline tracing. Evvard and Malsen provide an early discussion on the use of streamline tracing for inlet geometry [15]. For the purposes of creating a supersonic inlet, the streamline tracing technique integrates streamlines through a compressive, supersonic flowfield to generate a contour surface that can be used as the physical geometry of a supersonic inlet [16–18]. Evvard and Malsen's motivation for using this technique was due to the complexity of the three-dimensional method of characteristics. Instead of mapping an unknown flowfield for a known geometry, they chose to define a flowfield and determine the geometry that would correspond to that known flowfield [15].

An example of a streamline-traced inlet (STI) is the Busemann inlet. The Busemann inlet is an axisymmetric inlet derived from an axisymmetric, isentropic compression field that terminates in a conical shock. Studies of STIs have explored the design, application, performance of the Busemann inlet, including variants that involve truncating the parent flowfield, as a hypersonic inlet [19–25]. Another example of a STI comes from application

of Oswatitsch's conclusion in [26]. Oswatitsch found for a number of deflection surfaces, the optimum total pressure recovery occurs for the Mach numbers normal to their respective shock waves are equal, that is to say, the oblique shocks are of equal strength. If we extend this concept to an infinite number of deflection surfaces, the strength of a single shock wave in this configuration would be infinitesimal. Additionally, the flow would still turn and compress. The contour of this compression surface can be considered the streamline-trace of an isentropic compression field.

These two examples share a common feature beyond being STIs in that they both feature isentropic compression. The consideration of isentropic compression with an inviscid, supersonic flow is a reason why STIs are interesting. The conventional supersonic inlets mentioned above do all of their compression when the flow moves across one or a number of shock waves. When the flow moves across a shock wave, the total pressure decreases and entropy increases. These are both representations of losses via a decrease in the total internal energy of the flow. in the form of less work being able to be extracted from the flow when it reaches the energy extraction phase of the propulsion unit. As the flow cross a shock wave, heat transfer must occur. This is represented in the decrease in the total pressure (a representation of available total internal energy) and an increase in entropy. The entropy is a representation of the energy lost due to the creation of heat. Entropy is considered a loss in this case because the internal energy of the flow converted to heat cannot be recovered [27, 28]. In contrast, the two examples of STIs presented do their compression (or at least most of the compression) of the flow in an isentropic manner, therefore, minimizing the total pressure loss and creation of entropy. This is a reason that makes STIs attractive for supersonic application in place of pitot, two-dimensional, or axisymmetric spike inlets. The increased performance of the STI comes at the cost of length and weight of the inlet. STIs tend to be longer and heavier than the previously mentioned inlet types. The length and weight of these inlets can be considerable factors in deciding to move forward with other inlet types.

3

1.2 Detonation Propulsion

Pressure-gain combustion has garnered much interest in recent years. This interest comes from seeking the theoretical thermodynamic efficiency gains of detonation over the deflagration mode of combustion. The first to attempt to describe a manner to harness detonations to produce work was by Humphrey in 1909 [29]. He described the heat addition phase of the thermodynamic cycle not as an isobaric process, like the Brayton cycle, but as an isochoric process, a constant volume process. This thermodynamic cycle has come to be eponymously known as the Humphrey cycle. In 1940, Zeldovich made note of the detonation process not being truly isochoric, but that the specific volume of the gas actually shrank by an amount during the heat addition phase [30]. While not stated explicitly in his work, the thermodynamic cycle described by Zeldovich is known as the Fickett–Jacobs cycle. The Fickett–Jacobs cycle has been largely used to describe the thermodynamic cycle of detonations [12,13,31,32].

As mentioned already, pressure gain combustion has been sought due to the gains to be had in thermodynamic efficiency. These gains can be seen by the differences between the Brayton and Fickett–Jacobs thermodynamic cycles. The steps of the Fickett–Jacobs thermodynamic cycle are as follows: isentropic compression, the detonation occurs adding heat to the system, adiabatic expansion, and heat rejection. It should be noted that the detonation process is not reversible. The Fickett–Jacobs cycle follows the Hugoniot curve during the heat addition portion of the cycle leading to a large increase in pressure and a reduction in the specific volume. The Brayton cycle restricts heat addition to a constant pressure process [12, 13, 31, 33]. Comparing the Brayton and Fickett–Jacobs cycles, one can see that due to the lack of constraint on the static pressure in the heat addition process the Fickett–Jacobs cycle can be used to produce more work [12, 13].

Other cycles have been proposed to better capture the natural phenomenon of detonations. The structure of detonation waves is described by the Zeldovich–von Neumann–Döring (ZND) theory. Figure 1 shows an example of a p–v diagram of the detonation process as described by ZND theory.
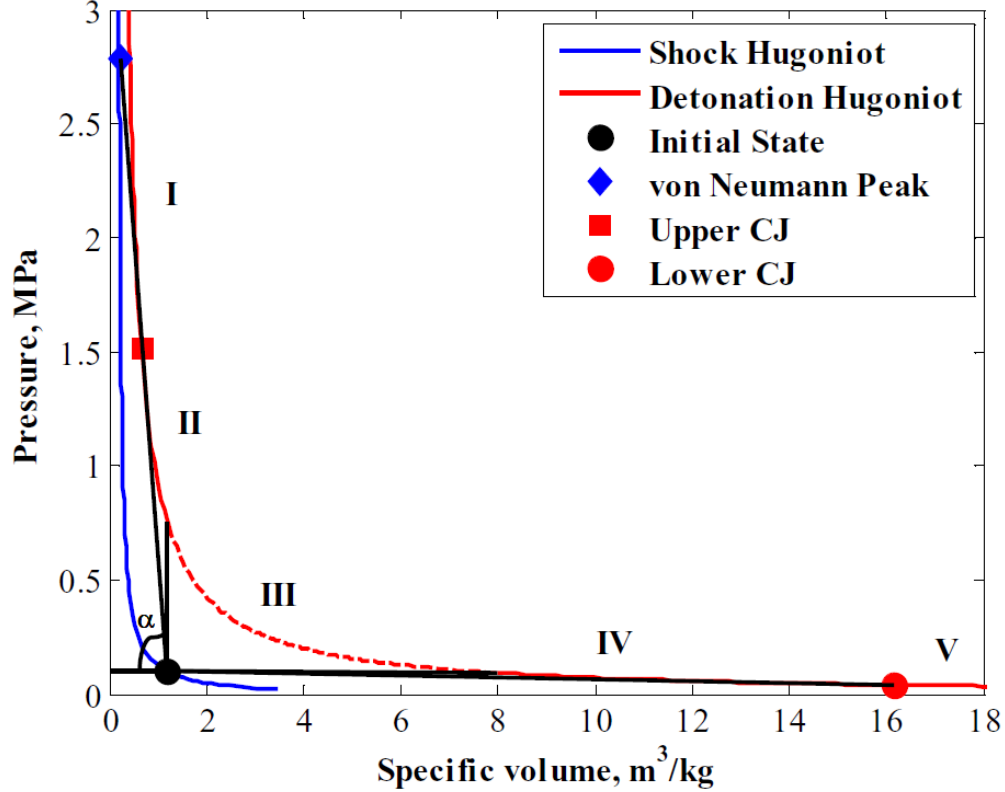
Figure 1: Real gas Hugoniot curves for stoichiometric hydrogen–air combustion from [34]

As the state of the gas advances from the initial state to the von Neumann peak, the state is described by the shock Hugoniot. The detonation wave consists of a planar shock traveling at the detonation velocity and leaves behind heated and compressed gas. An induction period follows after the planar shock which the chemical reaction of the fuel and oxidizer begins. During the reaction, the temperature and density increase until each value moves from the values at the von Neumann peak to the upper Chapman–Jouguet (CJ) point where the reaction attains equilibrium. A rarefraction wave follows behind the chemically reacting zone where the state of the gas moves from the upper CJ point to the lower CJ point. The static pressure decreases as the specific volume increases sharply [35]. From the structure of the detonation wave, one can construct a thermodynamic cycle that follows the physical phenomena that make up the detonation. The thermodynamic cycle used to describe detonation has been called the Zeldovich–von Neumann–Döring (ZND) cycle [36,37]. For a known initial condition, the detonation increases in pressure and density along the

shock Hugoniot curve to the intersection with the Rayleigh line corresponding to the initial condition. This point is referred to as the von Neumann peak. The pressure and density decrease along the same Rayleigh line until the velocity of the gas is sonic. This is the upper CJ point and is defined by the Chapman–Jouguet condition: the gas velocity is exactly sonic based on conditions immediately downstream of the wave. The gas is assumed to expand adiabatically and isentropically until the pressure has reduced to the initial pressure. Constant pressure heat rejection concludes the cycle of a single detonation during which the density increases to the initial density and the heat added from the reaction is rejected from the system [35].

There are three dominant detonation-based engines in the literature: the oblique detonation wave engine (ODWE), pulse detonation engine (PDE), and the rotating detonation engine (RDE) [13, 38]. Previously called detonative ramjets [39, 40], most recently standing oblique detonation ramjet (SODramjet) [41], and among other names, ODWEs date back to the latter half of the 1940s [39, 40]. An ODWE consists of an oblique shock system and fuel feed upstream of a standing oblique detonation wave. The ODWE is attractive compared to the scramjet due to its short combustor length, less inlet diffusion, and simpler engine geometry. For a static geometry, the standing oblique detonation wave achieves design performance at a single altitude and freestream Mach number. Operation of ODWE at off-design conditions results in shock and detonation wave angles potentially missing the on-design cancellation surfaces. This can lead to sub-optimal performance or deflagration of the propellant. This problem is similar to oblique shock cancellation [42, 43]. The concept of PDEs is the repeated detonation of a premixed fuel/oxidizer mixture at either the open or closed end of a detonation chamber. There are many configurations of PDEs ranging from single-tube to multi-tube systems, valveless to mechanically-valved propellant feeds. A downside to PDEs is the reliable, repeated initiation of detonation at a frequency range of 10–100 Hz. The RDE principle consists of a detonation wave continuously propagating circumferentially through an annular detonation chamber. Over a range of operating condi-

tions, the RDE can reliably perform with little or no change to the engine annulus geometry unlike ODWE. In this way, the RDE is similar to PDE [13, 38].

In the late 1950s, two groups independently began studying the RDE. One group was at the University of Michigan [11, 44] and the other was at the Lavrentyev Institute of Hydrodynamics in the USSR [45]. An RDE consists of an annular combustion chamber where a detonation wave propagates circumferentially. The detonation is maintained by the constant feed of fuel and oxidizer in the axial direction from a mixing plenum. The detonation products expand in the axial direction toward the aft end of the combustion chamber until the gases exit the RDE to produce thrust [11, 44, 45]. In Wolański's comparison of pulse and rotating detonation engines, he points out that RDEs may be more easily utilized when compared to PDEs. This comes from the relative simplicity of the detonation initiation and ease of integration with existing turbomachinery [13]. It is also thought the pressure rise in the detonation engine may be able to eliminate (or at least reduce) the need for a mechanical compressor, saving on weight and manufacturing costs. Overall, the configuration of the RDE appears to lend itself to a compact, widely scalable combustion unit [38, 45–48]. Work on the cycle analysis and design of RDEs has progressed in the past decade [49–52]. This has led to models that allow for relatively quick parametric design of an RDE.

As RDE technology matures, studies coupling an RDE with other propulsion system components have begun to take place. Numerical, analytical, and experimental studies have been performed with an RDE and a gas turbine [48, 53–55]. Paxson and Naples discussed the coupling between a successfully coupled RDE and a gas turbine [54]. Welsh et al. successfully determined the performance of the coupled RDE and gas turbine allowing for further steps towards designing for improved performance. Some have noted that there has been a shift of interest from PDEs to RDEs because of the practicality of detonation initiation occurring only once in an RDE whereas detonation initiation for PDEs must occur consistently throughout the operation of the engine [53]. Rankin et al. claimed that their RDE coupled with a gas turbine achieved similar or better performance than a conventional

7

gas turbine engine across a range of operating conditions [55].

Studies of RDEs coupled with inlets have also been conducted. Frolov et al. successfully demonstrated an air-breathing, continuous detonation engine in a wind tunnel [56, 57], although the reported freestream total temperature may be too low for realistic operation. Mizener et al. performed an analytical performance sensitivity study for RDEs coupled with two-dimensional waverider forebodies [58]. Bedick et al. were able to develop a laboratory-scale experimental testing platform to specifically test inlets for RDEs [59].

1.3   Motivation and Research Objectives

As rotating detonation engines (RDEs) gain popularity, studies are needed investigating the interactions between the RDE and other propulsion system components. The recent heightened interest in RDEs has led to more studies on the fundamentals and operation of the RDE, but the current literature has just recently started to expand the breadth of RDE research to include studies where an RDE is coupled with other propulsion components [31, 48, 60, 61]. Currently, the majority of RDE coupled with other propulsion components is dominated by studies focused on power extraction from the flow downstream of the RDE [53, 54, 62, 63]. Some studies for integrated inlet/RDE systems do exist, but are rarer in the literature [56–58]. The present study aims to expand the literature available on integrated inlet/RDE systems.

As RDE technology matures, knowledge of how the engine performance is affected by other propulsion equipment will be crucial. This study starts at the front end of a high-speed propulsion system by integrating the RDE with a supersonic inlet. Adding to the knowledge-base aids in bringing airbreathing RDEs into reality.

A two-dimensional, streamline-traced inlet (STI) is designed. The inlet performance is calculated and an optimum inlet design is selected. Off-design inlet performance is also calculated. The inlet exit conditions are fed into a low-order RDE model to determine the performance sensitivities of the integrated system at on- and off-design conditions at the

flight altitude.

Two streamline-traced inlets are designed to determine the performance of the integrated STI/RDE system. The STIs are designed for high total pressure recovery and volumetric efficiency. For the RDE, it is desired to achieve high thrust, high fuel-based specific impulse, low resultant torque, and low thrust-based fuel consumption. The performance sensitivities of the RDE are to be determined for:

1. Two different STIs at on-design conditions,

2. Two different STIs at off-design conditions, and

3. For items 1 and 2 utilizing two different fuels, namely, hydrogen and propane, for a parametric sweep of of RDE size.

The outcome of this study will produce a combination of STI geometry, RDE size, and fuel choice for a range of flight Mach numbers for the STI.

2   Numerical Methods

2.1   Method of Characteristics

To design an STI, a parent flowfield must be known with established flow structures and boundary conditions. Two-dimensional gasdynamics relations can be used to predict the flow properties at some locations in the inlet, but not throughout the entire flowfield. To evaluate the flow properties throughout the truncated isentropic compression flowfield (see §3.2 for more on the parent flowfield architecture), the two-dimensional method of characteristics (MOC) is used.

MOC is a technique for determining flow properties from information in the upstream and is, therefore, a method that is apt for purely supersonic flows. The flow is solved by determining the properties at the intersections of characteristic lines from compatibility equations. For irrotational flow, the characteristic lines are the Mach lines. The slopes of the left-running (positive slope) and right-running (negative slope) characteristic lines are

$$\lambda_\pm = \tan\left(\theta \pm \mu\right) \tag{1}$$

For two-dimensional, inviscid, irrotational, steady flow, the compatibility equations are

$$K_\pm = \theta \mp \nu = \text{constant} \tag{2}$$

Note that $K_+ \neq K_-$, but they are constant along their respective characteristic lines. As the characteristic lines project downstream, their intersections inform the local flow conditions.

2.1.1   Initial Data Line

To begin evaluation of the flow by MOC, an initial data line of known flow properties must be established. In the case of the STI, the initial value line is taken to be a left-running characteristic line originating from the initial deflection wedge and terminating at the initial

oblique shock wave, which is located very close to the leading edge of the STI body, assuming an incoming flow from left to right. The initial data line is assumed to have the post-shock flow properties determined by oblique shock theory. For example, the green line in Figure 2 is an initial value line [27, 28, 49, 64–67].
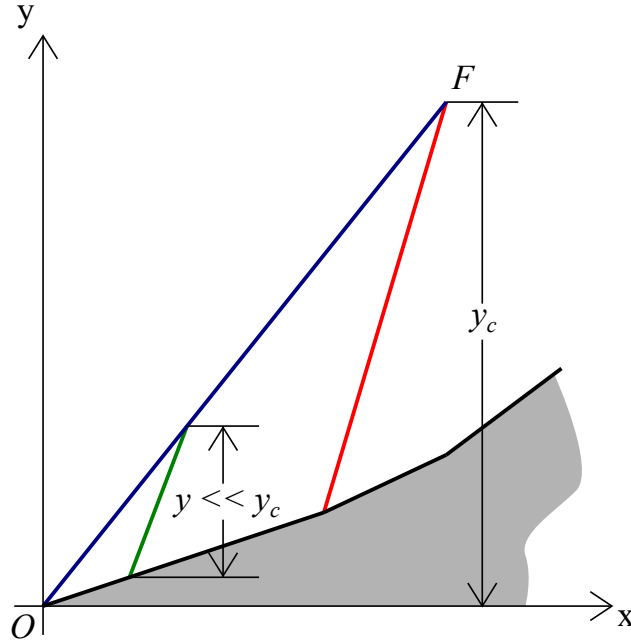
Figure 2: Example of a method of characteristics initial value line (the green line)

2.1.2 Unit Processes

In general, MOC is made up of a number of unit processes where the flow properties are determined by considering the information from the upstream and the local boundary conditions. For the current inlet study, three unit processes are used to determine the properties of the internal, wall, and shock points, respectively.

Internal Points

As shown in Figure 3, an internal point (point 3) is where a left-running characteristic line (line 23) intersects with a right-running characteristic line (line 13). At this intersection, the characteristic constants $(K_-)_1$ and $(K_+)_2$ are known from the upstream points (points

1 and 2 respectively) and they satisfy the compatibility equations

$$(K_-)_3 = \theta_3 + \nu_3 = (K_-)_1 \tag{3a}$$

$$(K_+)_3 = \theta_3 - \nu_3 = (K_+)_2 \tag{3b}$$
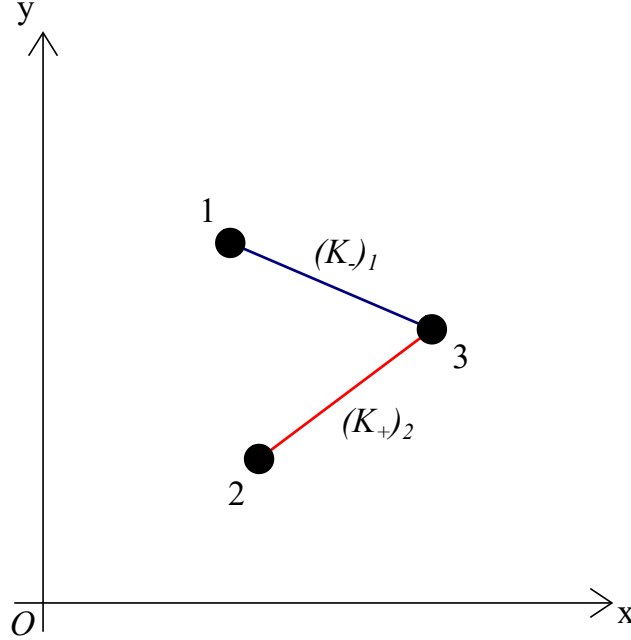
Figure 3: Diagram of a MOC internal point

The local flow and Prandtl–Meyer angles are then determined by

$$\theta_3 = \frac{1}{2} \left[(K_-)_1 + (K_+)_2 \right] \tag{4a}$$

$$\nu_3 = \frac{1}{2} \left[(K_-)_1 - (K_+)_2 \right] \tag{4b}$$

With ν_3 known, the local Mach number can be determined by Hall's method [68]. Other local flow properties can then be determined [27, 28, 64, 66].

Wall Points

Figure 4 considers a point (point 5) located at a wall, that is, the inlet body. The right-running characteristic constant $(K_-)_4$ is known from the upstream (point 4), and the local

12

flow angle, θ_5, is equal to the wall inclination. From Equation (2), the Prandtl–Meyer angle at the wall can be determined by

$$\nu_5 = (K_-)_4 - \theta_5 = \nu_4 + \theta_4 - \theta_5 \tag{5}$$

The left-running characteristic from point 5 is then calculated by equation (2) [27,28,64,66].
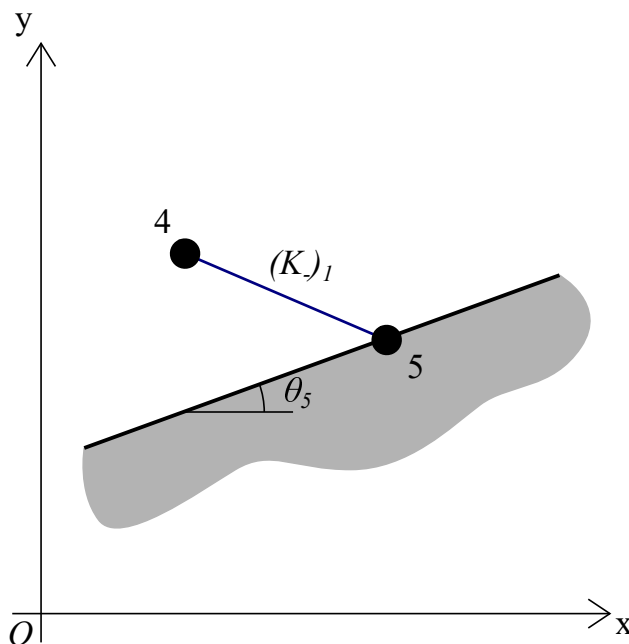
Figure 4: Diagram of a MOC wall point

Shock Points

Figure 5 shows a point (point 7) located immediately downstream of an oblique shock. To determine the flow properties at point 7, the freestream Mach number M_∞ and the left-running characteristic constant $(K_+)_6$ must be known. By iterating β_7, the flow angle at point 7 θ_7 is calculated by

$$\tan \theta = 2 \cot \beta \left[\frac{M^2 \sin^2 \beta - 1}{M^2 (\gamma + \cos 2\beta) + 2} \right] \tag{6}$$
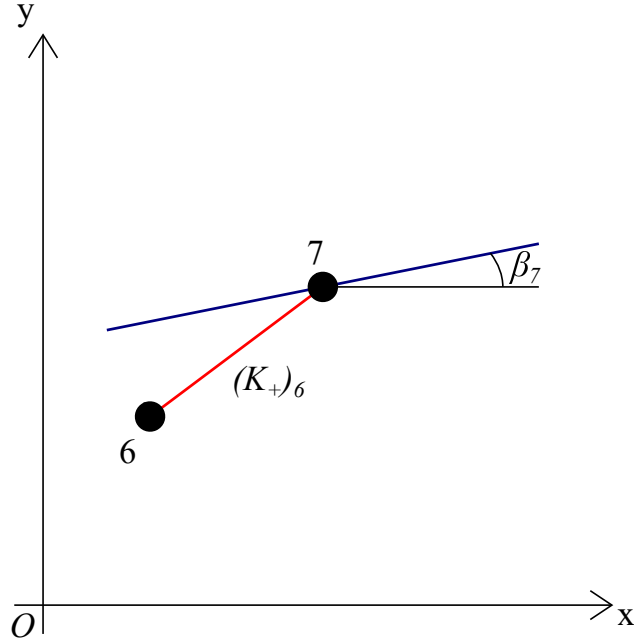
Figure 5: Diagram of a MOC shock point

With the flow angle θ_7, the Mach number M_7 is calculated by equation (19), and the Prandtl–Meyer angle ν_7 by equation (29). Convergence is achieved if the left-running characteristics are equal, namely, $(K_+)_7 \equiv \theta_7 - \nu_7 = (K_+)_6$.

2.1.3 Execution of MOC Algorithm

With the three unit processes above, the flow properties for the entire compression system encompassed by the leading oblique shock, the reflected shock separating the external and internal compression systems, and the inlet body can be determined by executing MOC as follows [27, 28, 64, 66].

The algorithm can be seen in flowchart form in Figure 6. The initial data line along the left-running characteristic line for a specified number of points n is established in Figure 7a. The right-running characteristic from the point nearest the STI body (point "A2" in Figure 7) is cast to the STI body. The intersection of the characteristic line and the STI body is recorded as the first point of a new solution line in Figure 7b. For the $(n-2)$ internal points in the new solution line, the left-running characteristic comes from the previous point from

the solution line and the right-running characteristic comes from the previous solution line. For example, in Figure 7c, point "B2" comes from points "B1" and "A3," and point "B3" comes from points "B2" and "A4." The internal point unit process is executed for each of the new internal points in sequence. The shock point is determined by the intersection of the left-running characteristic line and the the oblique shock in Figure 7d.
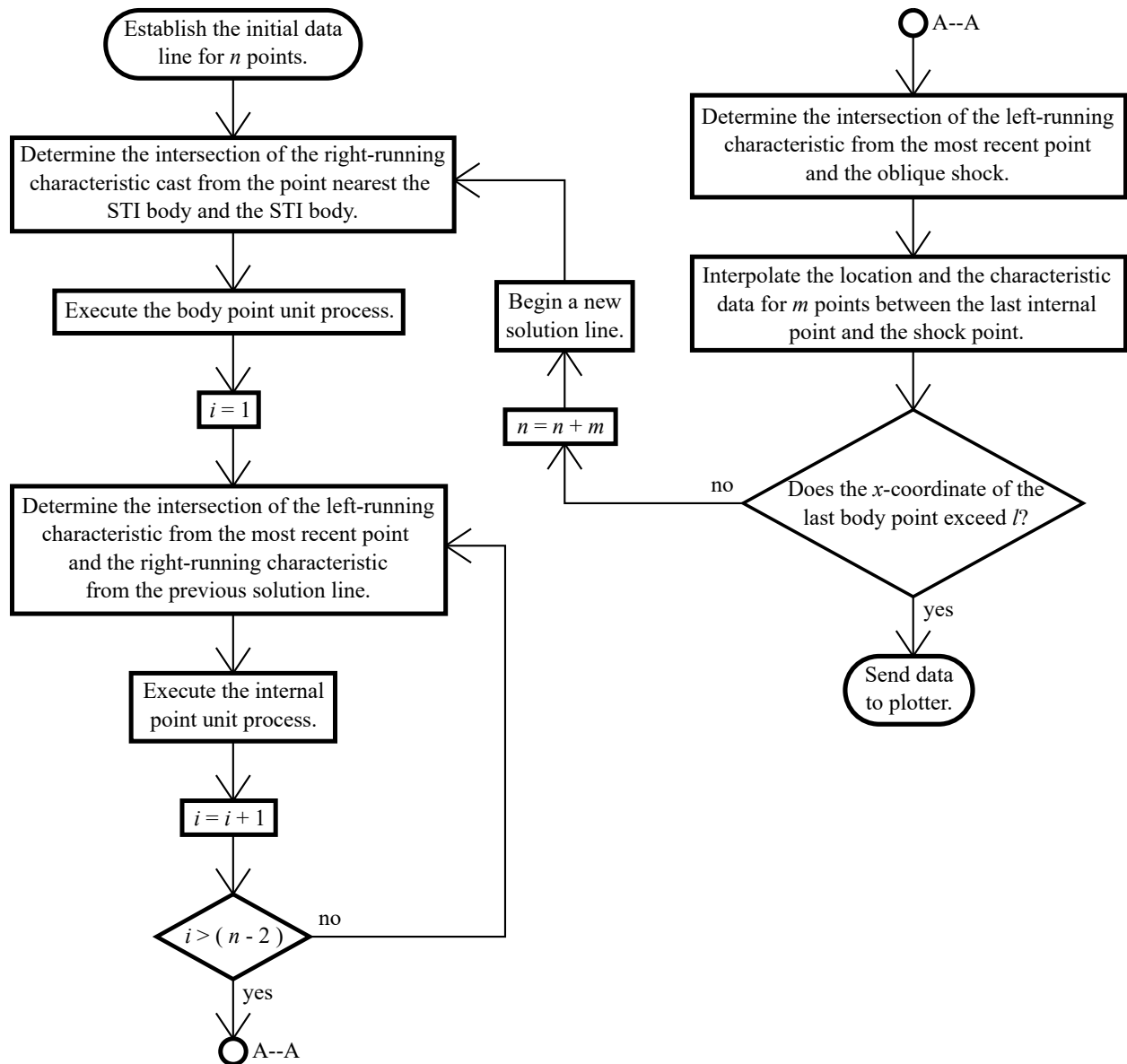
Figure 6: Algorithm flowchart for the execution of the method of characteristics
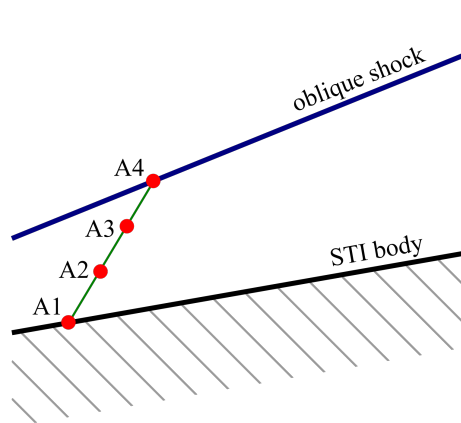
(a) Establish the initial data line for n points
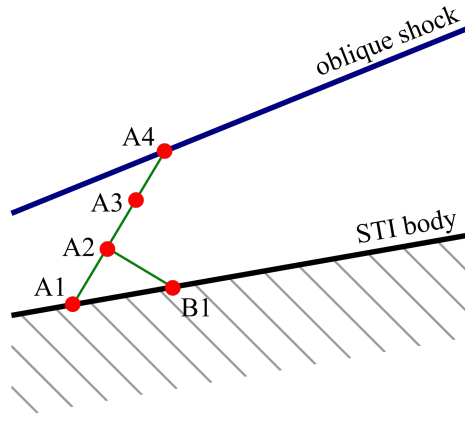
(b) Execute the body point unit process
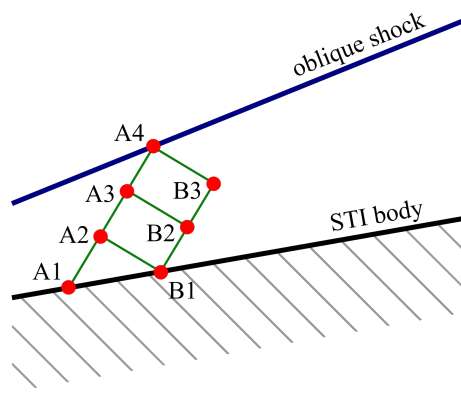
(c) Execute the internal point unit process for $n-2$ points
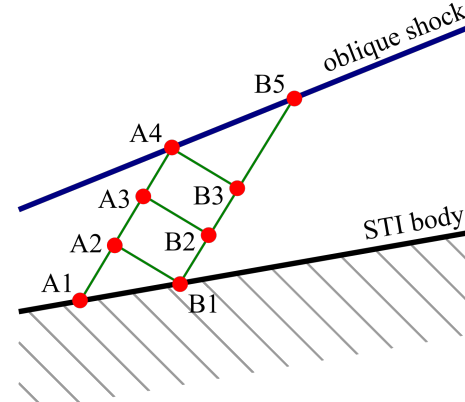
(d) Execute the shock point unit process
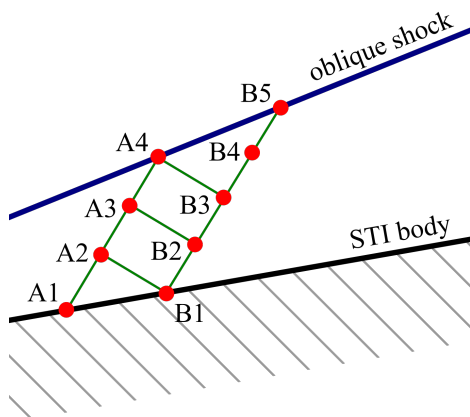
(e) Interpolate m points between the last internal point and the shock point along the left-running characteristic line
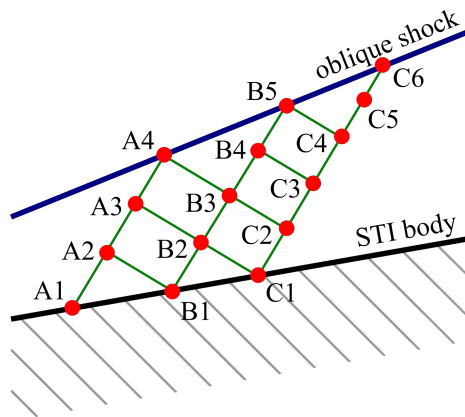
(f) Repeat steps shown in Figures 7b–7e until the entire flowfield is solved

Figure 7: Illustrations outlining the execution of the MOC algorithm

Notice in Figure 7d that the space between the last internal point "B3" and the shock point "B5" is much larger than the space between other points in the same solution line. If this were to be left as is, gaps in the data points would begin to propagate downstream. To prevent the diffusion of solution points, additional m internal points are added between the last internal point and the shock point by interpolation. At this point, the x-coordinate of the last body point is compared to the inlet length, l. If $x_{body} \geq l$, the program ends and the data is plotted and saved. If $x_{body} < l$, a new solution line is begun where $n = n+m$. Because this method is terminated when the body point exceeds the length, there are a number of data points downstream that are invalid. These points are removed from the data-set before plotting.

2.2   Computational Fluid Dynamics Framework

Numerical analysis was conducted to evaluate the STI performance employing the Euler equations, so that transport processes are ignored. The conservation equations of mass, momentum, and energy are therefore

$$\frac{\partial \rho}{\partial t} + \nabla \cdot (\rho \mathbf{u}) = 0 \tag{7}$$

$$\frac{\partial}{\partial t} (\rho \mathbf{u}) + (\mathbf{u} \cdot \nabla) \rho \mathbf{u} = -\nabla p \tag{8}$$

$$\frac{\partial}{\partial t} (\rho e_t) + \nabla \cdot (\rho e_t \mathbf{u}) = -\nabla \cdot (p \mathbf{u}) \tag{9}$$

where the specific total energy is
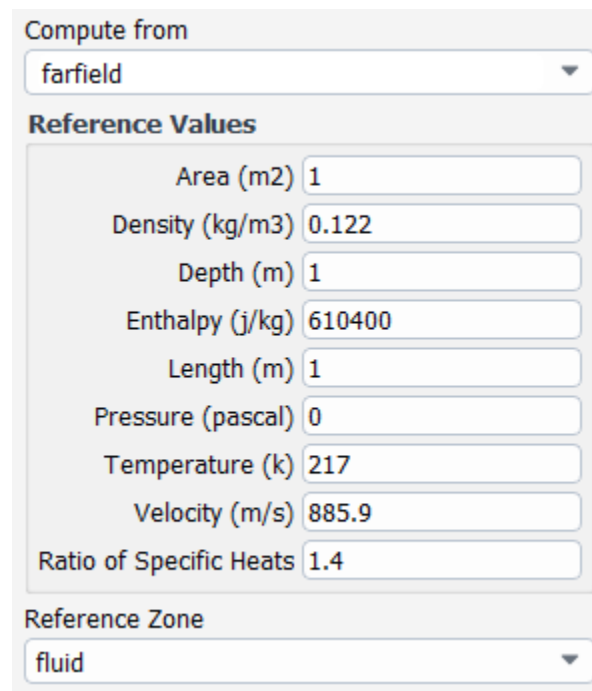
$$e_t = e + \frac{u^2 + v^2}{2} \tag{10}$$

There are four equations (the momentum equation (8) can be split into two equations) and five unknowns: ρ, u, v, p, and e. To complete a solvable set of equations, the ideal gas law is employed as the state equation

$$p = \rho R T \tag{11}$$

17

where R is the specific gas constant. The specific internal energy e can be approximated by a polynomial function of temperature T [69].

The commercial computational fluid dynamics package ANSYS Fluent® is employed in this study. The two-dimensional, steady Euler equations are solved using a coupled, implicit, second-order upwind solver applied to a steady-state model. The flux term is discretized by the advection upstream splitting method. The conservation equations are coupled by using a density-based solver. The working fluid used is air set to be treated as a thermally perfect gas. Figure 8 is a screenshot of the reference values in Fluent® applied to the farfield gas.

Compute from
farfield ▼

Reference Values

Area (m2)	1
Density (kg/m3)	0.122
Depth (m)	1
Enthalpy (j/kg)	610400
Length (m)	1
Pressure (pascal)	0
Temperature (k)	217
Velocity (m/s)	885.9
Ratio of Specific Heats	1.4

Reference Zone
fluid ▼

Figure 8: Reference values in Fluent®

In Fluent®, the farfield gas is treated as a boundary condition where the air far from the STI (upstream, to the side, and downstream) is assumed to be undisturbed by the presence of the STI in the flow. At the boundary, the reference values in Figure 8 describes the state of the air in the farfield at the test case altitude and Mach number. Fluent® uses the reference values to determine the state of the air at locations other than the farfield via the chosen gas model in the computation process. For the reference values, the state of the air is taken

from the 1976 U.S. Standard Atmosphere [70] and is discussed in §3.1. The "depth" is the width of the two-dimensional inlet, $w = 1.0$ m. The "area" is specified as the capture area of the inlet, $A_c = y_c w = 1.0$ m^2. The "length" is a characteristic length. For simplicity, the reference pressure is set as zero, and the values of the absolute pressure are used during the computation. The "enthalpy" is the specific total enthalpy determined by

$$h_{t,\infty} = c_p T_\infty + \frac{1}{2} V_\infty^2 \qquad (12)$$

where the subscript ∞ refers to the undisturbed far upstream conditions.

3 Design of STI

3.1 Design Conditions

Two STIs are designed in the course of the study. A common design condition is chosen for both STIs. All cases considered are at a geometric altitude of 18 km. The state of the air is taken from the 1976 U.S. Standard Atmosphere [70]: static pressure $p_\infty = 7\,570$ Pa, static temperature $T_\infty = 217$ K, and density $\rho_\infty = 0.122$ kg/m^3.

$$T_{t,\infty} = T_\infty \left(1 + \frac{\gamma - 1}{2} M_\infty^2 \right) \tag{13}$$

$$p_{t,\infty} = p_\infty \left(1 + \frac{\gamma - 1}{2} M_\infty^2 \right)^{\gamma/(\gamma-1)} \tag{14}$$

The air far upstream from the STI is assumed to be uniform. At the design Mach number $M_\infty = 3.0$, the total pressure $p_{t,\infty} = 278\,000$ Pa and total temperature $T_{t,\infty} = 608$ K.

Table 1: Summary of design conditions and specifications for both STIs

Altitude	18	km
p_∞	7 570	Pa
$p_{t,\infty}$	278 000	Pa
T_∞	217	K
$T_{t,\infty}$	608	K
ρ_∞	0.122	kg/m^3
M_∞	3.0	—
M_ω	1.2	—
u_∞	885.8	m/s
v_∞	0.0	m/s
q_∞	47 860	Pa
w	1.0	m
y_c	1.0	m

3.2 Parent Flowfield Architecture

The parent flowfield chosen for the STI development is an isentropic compression flowfield. This type of flowfield is chosen to minimize total pressure loss along the inlet. Designating

the flowfield as isentropic does not sufficiently define the shape of the flowfield; the shape of the flowfield must be specified. The Busemann flowfield is taken as a template to shape the parent flowfield. In the present work, two changes are made to the original Busemann flowfield. First, instead of axisymmetric, the flowfield is restricted to be two-dimensional, planar. Second, the symmetry with respect to the centerline is abandoned. Figure 9 shows the fully developed parent flowfield in the present work.
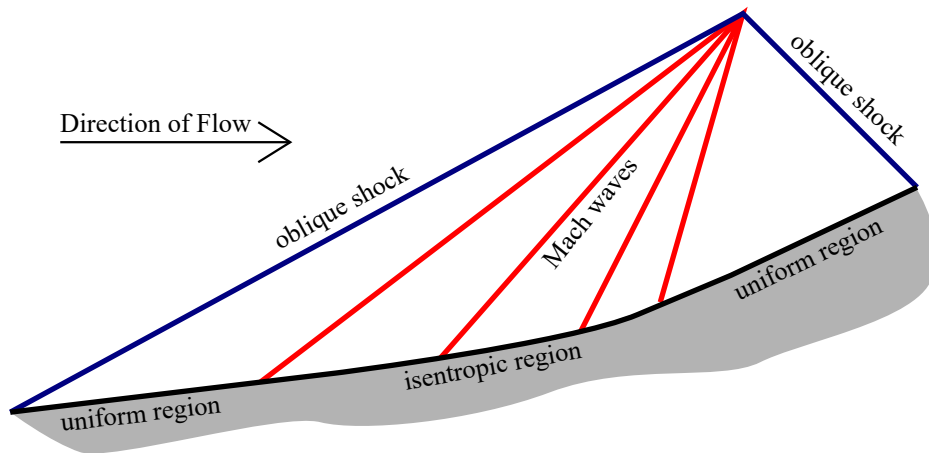
Figure 9: Illustration of the parent flowfield

The isentropic flowfield begins in the same direction as the freestream flow. The flow is isentropically turned, casting off Mach waves as the flow is compressed. The contour of the flowfield is shaped in a way to where all of the Mach waves intersect at a single point, the focus. The flow is turned back to the freestream direction by an oblique shock wave. A disadvantage of Busemann inlets is their excessive length, leading to extra weight amongst other penalties. This disadvantage has led to studies to attempt to truncate the Busemann flowfield with minimal loss in performance [71–73]. Truncating the flowfield requires the flowfield to begin with an oblique shock. To maintain the Mach waves intersecting at the focus, a uniform flow region on either side of the isentropic compression region must be introduced.

The STIs being considered are mixed compression inlets. These inlets incorporate an external and an internal compression system. The truncated two-dimensional, isentropic

compression flowfield is used for the external compression system of the STIs. Two internal compression system configurations are considered: single-sided compression and symmetrical compression. In the present work, the STI incorporating the single-sided compression is called "STI–1" and the STI incorporating the symmetrical compression is called "STI–2." These labels are maintained for the remainder of this study.

(a) Single-sided compression   (b) Symmetrical compression
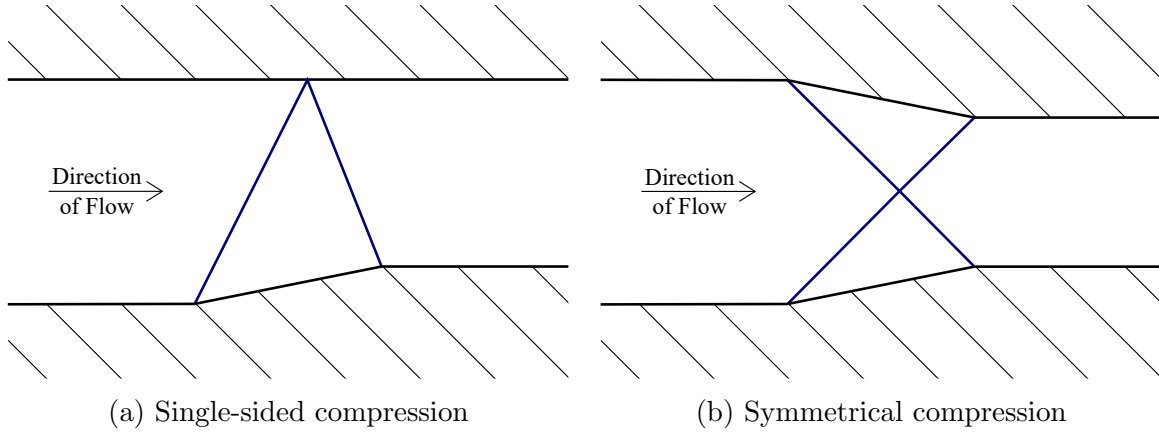
Figure 10: Illustrations of internal compression systems

3.3 Performance Metrics

Two performance metrics were chosen for the STI design: the total pressure recovery π and the volumetric efficiency $\eta_\mathbb{V}$. The total pressure recovery is a typical inlet performance metric, which measures how much available total pressure remains in the flow after passing through the inlet. Maximizing the total pressure recovery (or minimizing the energy loss of the flow) is synonymous to achieving a better performing inlet.

The volumetric efficiency is a modified ratio of the volume, $\mathbb{V}$, to the wetted surface area, s_w. The volumetric efficiency is given by

$$\eta_\mathbb{V} = \frac{\mathbb{V}^{2/3}}{s_w} \tag{15}$$

In general, large volumes are preferred to accommodate internal structures, fuel, and payload storage, and at high speeds, minimization of the wetted surface area is attractive to minimize

convective heating on the vehicle. Therefore, maximizing the volumetric efficiency is the intended performance outcome.

Figure 11 shows the schematic of an inlet flowfield. The solid red lines are oblique shock waves. The dashed red lines mark the borders of an isentropic compression region. The solid blue line shows the termination shock. The total pressure decreases as the flow moves across the shocks, namely $\infty \to 1$, $2 \to 3$, $3 \to 4$, but remains constant in the isentropic region.
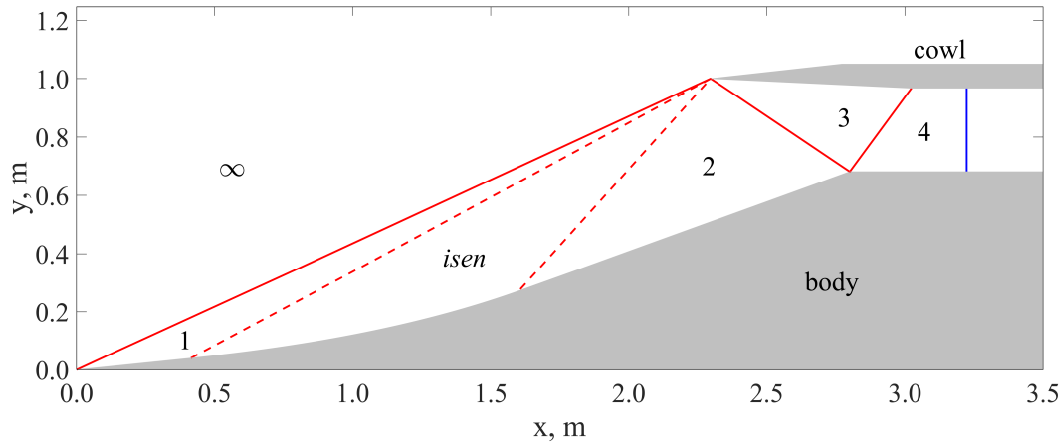
Figure 11: Schematic of an STI

The total pressure recovery across the inlet in Figure 11 is

$$\pi = \frac{p_{t,1}}{p_{t,\infty}} \frac{p_{t,isen}}{p_{t,1}} \frac{p_{t,2}}{p_{t,isen}} \frac{p_{t,3}}{p_{t,2}} \frac{p_{t,4}}{p_{t,3}} \tag{16}$$

$$= \frac{p_{t,1}}{p_{t,\infty}} \frac{p_{t,3}}{p_{t,1}} \frac{p_{t,4}}{p_{t,3}} = \frac{p_{t,4}}{p_{t,\infty}} \tag{17}$$

noting that $p_{t,1} = p_{t,isen} = p_{t,2}$.

For a flow moving across an oblique shock wave, where i and j are the states upstream and

downstream of the shock respectively, the following pressure relationships can be written:

$$\frac{p_{t,i}}{p_i} = \left(1 + \frac{\gamma - 1}{2}M_i^2\right)^{\gamma/(\gamma-1)} \tag{18a}$$

$$\frac{p_j}{p_i} = 1 + \frac{2\gamma}{\gamma + 1}\left(M_{n,i}^2 - 1\right) \tag{18b}$$

$$\frac{p_{t,j}}{p_j} = \left(1 + \frac{\gamma - 1}{2}M_j^2\right)^{\gamma/(\gamma-1)} \tag{18c}$$

$$\frac{p_{t,j}}{p_{t,i}} = \frac{p_{t,j}}{p_j}\frac{p_j}{p_i}\frac{p_i}{p_{t,i}} \tag{18d}$$

where

$$M_{n,i} = M_i \sin\beta \tag{19a}$$

$$M_{n,j}^2 = \frac{M_{n,i}^2 + \dfrac{2}{\gamma - 1}}{\left(\dfrac{2\gamma}{\gamma - 1}\right)M_{n,i}^2 - 1} \tag{19b}$$

$$M_j = \frac{M_{n,j}}{\sin(\beta - \theta)} \tag{19c}$$

Viable STI designs must satisfy the minimum total pressure recovery specified in [74].

$$\pi_{min} = 1.0 - 0.075\left(M_\infty - 1\right)^{1.35} \tag{20}$$

where the freestream Mach numbers range from 1 to 5. There are minimum total pressure recoveries for freestream Mach numbers below 1 and above 5, but they are not relevant to the present investigation. This military specification is typically not difficult to meet in preliminary and conceptual designs, and acts as a traditional criterion for specifying the performance floor for an acceptable inlet design.

As stated before, large volumes with small wetted surface areas are the attractive combination for our application maximizing the volumetric efficiency. The STIs considered here are of a two-dimensional, planar geometry so that equation 15 has to be modified appropri-

ately. Let the area A be the cumulative area of the body and cowl of the inlet (the grey shapes in Figure 11) and the inlet width be the unit width, then the STI volume is

$$\mathbb{V} = Aw \tag{21}$$

The wetted surface area is the area that is exposed to the flow. The contour length of the inlet body and cowl surfaces multiplied by the inlet width yields the wetted surface area of the specific STI design. The inlet contour length was formulated as a summation. Let the contour length of a single segment of the inlet body or cowl be

$$s_i = \sqrt{(x_i - x_{i-1})^2 + (y_i - y_{i-1})^2} \tag{22}$$

Then the wetted surface area of the STI is

$$s_w = w \left[\left(\sum s_i \right)_{body} + \left(\sum s_j \right)_{cowl} \right] \tag{23}$$

Hence

$$\eta_{\mathbb{V}} = \frac{(Aw)^{2/3}}{w \left[\left(\sum s_i \right)_{body} + \left(\sum s_j \right)_{cowl} \right]} \tag{24}$$

3.4 Development of STI Geometry

The STI geometry is defined by the inlet capture height y_c, freestream Mach number M_∞, initial deflection angle θ_1, isentropic compression turning angle $\Delta\theta$, Mach number at the entrance of the internal compression system M_3, and the terminal Mach number M_ω. As mentioned before, the design case set M_∞. The length of the inlet geometry is parameterized by y_c. It can be noted that inlets where the flow is sufficiently slowed to low supersonic Mach numbers would be attained by specifying M_ω. Furthermore, inlets where the flow is sufficiently slowed to low supersonic Mach numbers are found to be more easily attained by varying M_3 instead of $\Delta\theta$. Therefore, in the present work, the independent variables are

chosen to be y_c, M_∞, and M_ω, and the design parameters are chosen to be θ_1 and M_3. The optimal inlet candidate can be determined over the parametric design space.

The STI begins with an acute deflection surface at angle θ_1. This angle is the truncation angle of the isentropic compression field mentioned in §3.2. With M_∞ and θ_1, the oblique shock angle β is determined from

$$\lambda = \left[\left(M^2 - 1 \right)^2 - 3 \left(1 + \frac{\gamma - 1}{2} M^2 \right) \left(1 + \frac{\gamma + 1}{2} M^2 \right) \tan^2 \theta \right]^{1/2} \tag{25a}$$

$$\chi = \frac{\left(M^2 - 1 \right)^3 - 9 \left(1 + \frac{\gamma - 1}{2} M^2 \right) \left(1 + \frac{\gamma - 1}{2} M^2 + \frac{\gamma + 1}{4} M^4 \right) \tan^2 \theta}{\lambda^3} \tag{25b}$$

$$\tan \beta = \frac{M^2 - 1 + 2\lambda \cos \left(\frac{4\pi\delta + \cos^{-1} \chi}{3} \right)}{3 \left(1 + \frac{\gamma - 1}{2} M^2 \right) \tan \theta} \tag{25c}$$

where $\delta = 0, 1$ for the weak and strong shock solutions respectively. Only the weak solution is pertinent. With the deflection angle, upstream Mach number, and oblique shock angle, the Mach number behind the oblique shock is determined by equation (19), repeated here for convenience:

$$M_{n,i} = M_i \sin \beta \tag{19a}$$

$$M_{n,j}^2 = \frac{M_{n,i}^2 + \frac{2}{\gamma - 1}}{\left(\frac{2\gamma}{\gamma - 1} \right) M_{n,i}^2 - 1} \tag{19b}$$

$$M_j = \frac{M_{n,j}}{\sin \left(\beta - \theta \right)} \tag{19c}$$

The Mach angle

$$\mu = \sin^{-1} \frac{1}{M} \tag{26}$$

The deflection angle, oblique shock angle, and Mach angle create a triangle of uniform flow behind the oblique shock where the intersection of the oblique shock and Mach wave define

the focus of the parent flowfield described in §3.2. While the angles of the shock wave, Mach wave, and deflection surface define a triangular uniform flow region upstream of the isentropic compression region, these angles do not specify the size of this area. The size of this area can be determined in many ways. For example, the uniform flow region could be varied by the length of the initial deflection surface or by the height of the focus (or capture height). Specifying either of these dimensions will constrain the size of the uniform flow area. For this method, the uniform flow area is set to depend on the inlet capture height y_c. This is shown in Figure 12.
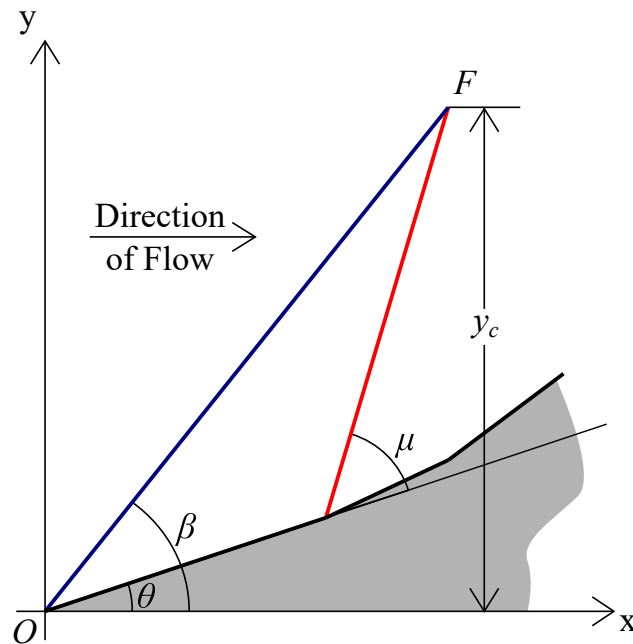
Figure 12: Diagram of the uniform-flow region upstream of
the isentropic compression flowfield

The location of the cowl lip is determined by

$$x_c = \frac{y_c}{\tan \beta_1} \tag{27}$$

The isentropic compression surface begins at the intersection of the leading Mach wave of the isentropic compression region and initial deflection surface. This point is determined by

$$x_1 = \frac{y_c - x_c \tan(\theta_1 + \mu_1)}{\tan\theta_1 - \tan(\theta_1 + \mu_1)} \tag{28a}$$

$$y_1 = x_1 \tan\theta_1 \tag{28b}$$

The Mach number downstream of the isentropic compression surface is determined from the Prandtl–Meyer angle there. The Prandtl–Meyer angle upstream is found by

$$\nu = \sqrt{\frac{\gamma+1}{\gamma-1}} \tan^{-1}\sqrt{\frac{\gamma-1}{\gamma+1}(M^2-1)} - \tan^{-1}\sqrt{M^2-1} \tag{29}$$

The maximum turning angle of the isentropic compression region is determined for the specified Mach number at the entrance of the internal compression system. By iterating through the turning angle, the Prandtl–Meyer angle and Mach number are found for the uniform flow region downstream of the isentropic compression region. With the turning angle of isentropic angle the Prandtl–Meyer angle downstream is

$$\nu_2 = \nu_1 - \Delta\theta \tag{30}$$

Hall's inverse Prandtl–Meyer scheme [68] is used to find the Mach number from the Prandtl–Meyer angle. The Mach number is then determined across the reflected shock separating the external and internal compression systems. The calculated Mach number is compared with the specified Mach number for the flow entering the internal compression system. Iteration of the isentropic turning angle continues if the Mach numbers do not equal or are not within a specified tolerance. The uniform flow downstream of the isentropic compression region is now known; the Mach number and flow direction are known. Through a second iterative process, the deflection angle(s) of the internal compression system are determined. A guess for the deflection angle is made. Equations (25) and (19) are used to determine the shock angle. Note, for the symmetrical internal compression system, this process must be performed twice.

The resultant Mach number across the shock structure is compared to the specified terminal Mach number. If the values do not equal or are not within an error tolerance a new guess for the deflection angle is made. The process is repeated until a deflection angle is found that results in the terminal Mach number being achieved. Figure 13 is a flowchart showing the two iteration loops.
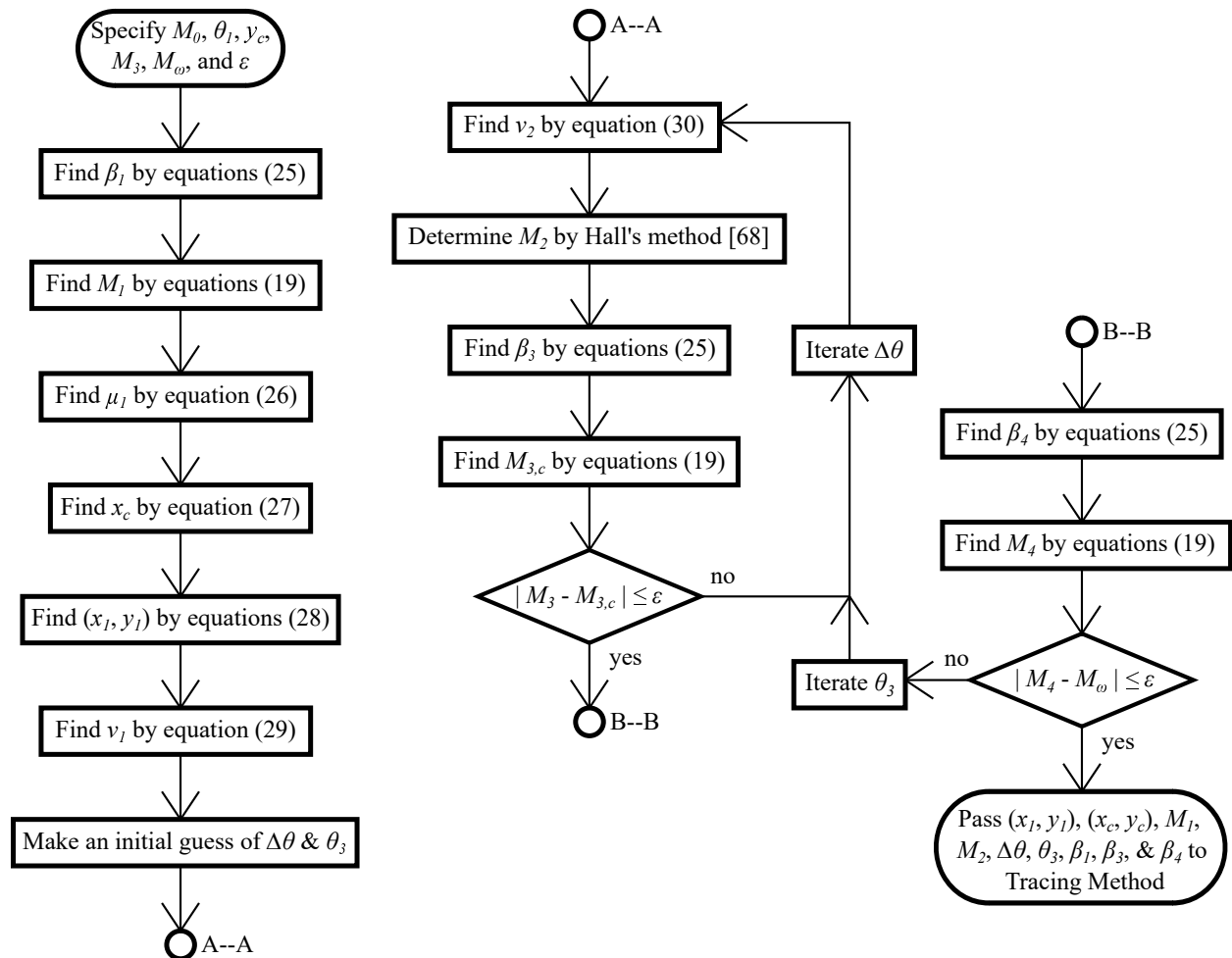
Figure 13: Algorithm to determine the parent flowfield for the STI

The Mach number and flow direction are now known throughout the STI excluding the isentropic compression region. The Prandtl–Meyer angles for the region immediately upstream and immediately downstream of the isentropic region are known. For a sufficiently large number of discrete surfaces to approximate the smooth contour of the isentropic region n, the difference in flow direction $d\theta$ is equal to $d\theta = \Delta\theta/n$. The streamline tracing of the

isentropic region is an iterative process. For the point i, the deflection angle and Prandtl–Meyer angle are

$$\theta_i = \theta_{i-1} + \mathrm{d}\theta \tag{31a}$$

$$\nu_i = \nu_{i-1} - \mathrm{d}\theta \tag{31b}$$

The location of the next point within the isentropic contour $(x_i,\, y_i)$ is determined by

$$x_i = \frac{y_{i-1} - y_c + x_c \tan\left(\theta_i + \mu_i\right) - x_{i-1} \tan\theta_i}{\tan\left(\theta_i + \mu_i\right) - \tan\theta_i} \tag{32a}$$

$$y_i = y_{i-1} + (x_i - x_{i-1}) \tan\theta_i \tag{32b}$$

The initial flow direction is the initial deflection angle, the initial Prandtl–Meyer angle is the Prandtl–Meyer angle immediately behind the initial oblique shock wave, and the initial values of $(x_i,\, y_i)$ are the endpoint of the initial deflection surface $(x_1,\, y_1)$. The intersection point of the initial oblique shock wave and all Mach waves is the focus and located at $(x_c,\, y_c)$. An illustration of the algorithm at work can be seen in Figure 14. The algorithm for the
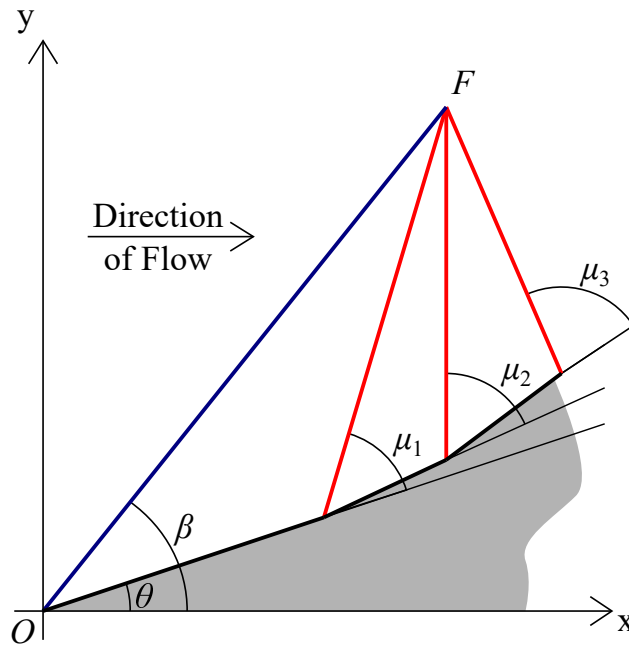
Figure 14: Diagram illustrating the streamline tracing in the isentropic region

streamline-tracing is shown in Figure 15.
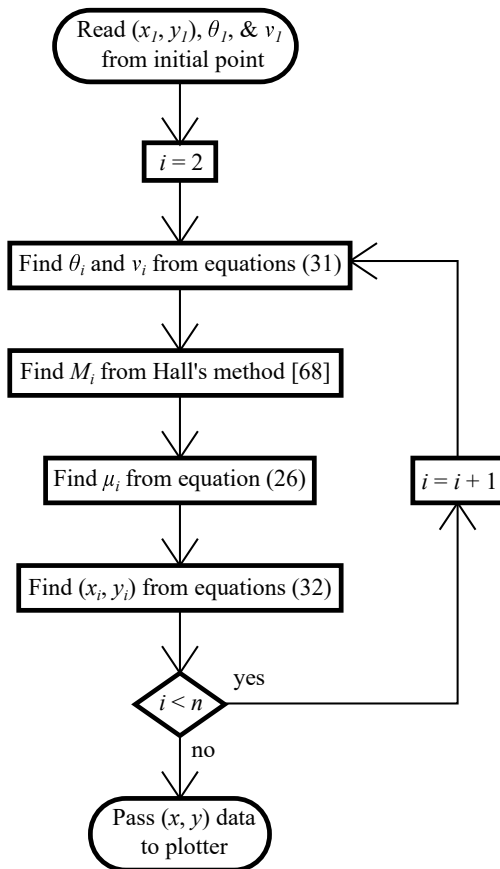
Figure 15: Algorithm for streamline-tracing in the isentropic compression region

The end point of the isentropic compression surface casts the remaining length of the external compression system toward the oblique shock separating the external and internal compression systems. The intersection of the surface and the reflected oblique shock is located at the inlet shoulder. The STI is now appropriately constrained between the capture height and the shock and deflection angles. A sample STI is seen in Figure 11.

With the chosen inlet capture height, freestream Mach number, and terminal Mach number, a family (or set) of STIs is defined by varying the initial deflection angle and Mach number at the entrance of the internal compression system. The initial deflection angle is varied from 4.0–11.0 deg in 0.5 deg increments for the initial parametric sweep. The Mach number located at the beginning of the internal compression system is varied from 1.30–1.70 in 0.05 increments for the initial parametric sweep. Each combination of the initial deflection

31

angle and Mach number at the entrance of the internal compression system represents a member of the STI family, referred as candidate STIs.

The performance metrics of the candidate STIs, that is, total pressure recovery and volumetric efficiency, are then evaluated. The performance sensitivity as a function of the design parameters is created, and a gradient descent optimization algorithm is applied to the inlet candidate data set [75]. Typically, this optimization algorithm finds local minima; however, if one chooses a negative step size this optimization method seeks the local maxima. This method is also called the steepest ascent or hill climbing optimization. Let

$$f = \begin{bmatrix} \pi\left(\theta_1,\ M_3\right) \\ \eta_{\mathbb{V}}\left(\theta_1,\ M_3\right) \end{bmatrix} \tag{33}$$

and

$$x = \begin{bmatrix} \theta_1 \\ M_3 \end{bmatrix} \tag{34}$$

Given an initial guess x_i, the next point x_{i+1} is determined by

$$x_{i+1} = x_i - \alpha \mathbb{H}\left(f\right) \cdot \nabla f \tag{35}$$

where α is the step size and $\mathbb{H}\left(f\right)$ is the Hessian matrix of f. This algorithm is repeated until $x_i - x_{i-1}$ falls below a specified tolerance. The final set of x is taken as the optimal STI design for the given internal compression system and design conditions.

3.5   Performance of STI–1

3.5.1   On-Design Conditions

STI–1 utilized the single-sided internal compression system. The parametric sweep in §3.4 was performed generating candidate STIs of varying performance. For the on-design case, a portion of those candidate STIs was found to have a total pressure recovery less than

the specified minimum in equation (20), that is, $\pi_{min}\left(M_\infty = 3.0\right) = 0.809$. The gradient ascent optimization was applied to the candidate STIs to find the optimal combination of total pressure recovery and volumetric efficiency. Table 2 shows the candidates with the maximum total pressure recovery and volumetric efficiency, and the final selection with the optimum performance combination. Figure 16 shows the optimum design in Table 2, denoted as STI–1. Table 3 presents the flow direction from the freestream to the exit plane.

Table 2: Inlet candidates for STI–1

	θ_1, deg	M_3	π	$\eta_\mathbb{V}$	l/y_c
π_{max}	4.0	1.30	0.852	0.119	3.13
$\eta_{\mathbb{V},max}$	11.0	1.30	0.819	0.134	2.57
Optimum	5.5	1.30	0.849	0.123	3.02
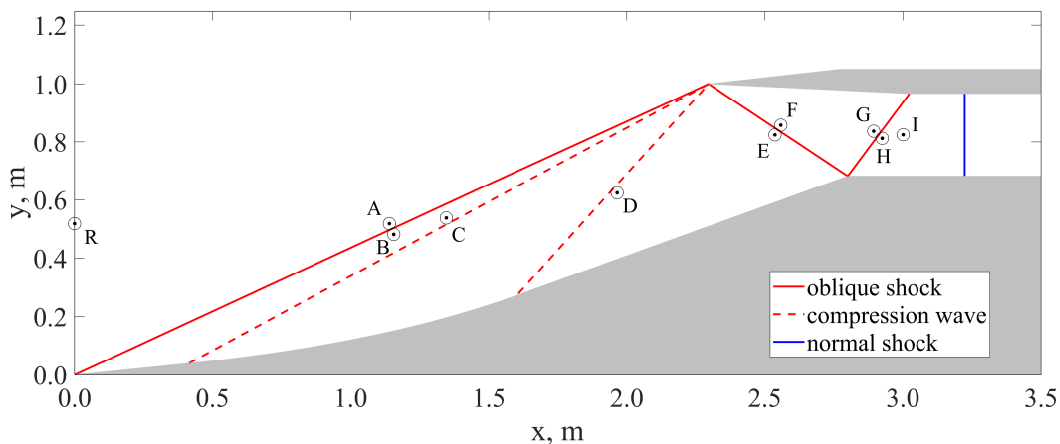
Figure 16: Schematic of STI–1 with associated shock structures

Table 3: STI–1 flow direction

Region	R–A	B–C	D–E	F–G	H–I
θ, deg	0.00	5.50	18.83	-2.61	0.00

To prepare for the off-design analysis for STI–1, the on-design case was then simulated in ANSYS Fluent® to verify if the CFD results are consistent with the theoretical solution.

The mesh was generated in Cadence Pointwise®. Figure 17 shows the specified boundary conditions.
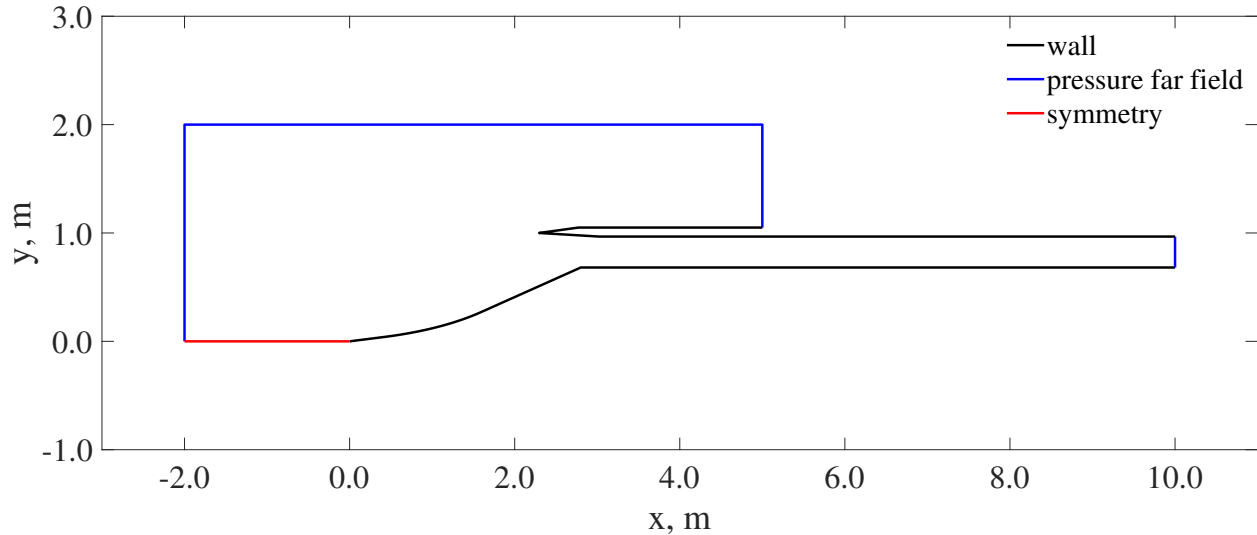
Figure 17: Boundary conditions and the domain extents of STI–1

Table 4 lists points upstream and within the STI where flow properties determined by the CFD model were compared to the theoretical solution. The listed points were offset 2.0 cm from the theoretical shock structures so that the point would be well within the uniform region and far enough away from the shock structure to avoid any possible smearing of the shock in the analysis. Ultimately, the distance from the shock structure was arbitrary. Points were set on both sides of each shock wave and the isentropic compression region. Note, point "R" was set in the freestream upstream of point "A" to verify that no issues arose in the freestream. These points can be seen in Figure 16.

Table 4: Locations of flow property monitors for STI–1

Station	x	y	Location description
R	0.00	0.52	Reference location upstream of Station "A"
A	1.14	0.52	Freestream condition; upstream of the initial oblique shock wave
B	1.16	0.48	Downstream of the initial oblique shock wave
C	1.35	0.54	Upstream of the isentropic compression region
D	1.97	0.62	Downstream of the isentropic compression region
E	2.54	0.82	Upstream of shock separating the external and internal compression systems
F	2.56	0.86	Downstream of shock separating the external and internal compression systems
G	2.89	0.84	Upstream of oblique shock reflecting from the inlet shoulder
H	2.93	0.81	Downstream of oblique shock reflecting from the inlet shoulder
I	3.00	0.83	Upstream of terminal normal shock

Table 5 shows the theoretical and CFD solutions to for the local Mach number, static pressure, and static temperature throughout STI–1. The difference fell below one percent. The CFD model predicted the total pressure recovery of 0.854, which was less than one percent different from the theoretical solution of 0.849.

To minimize the numerical uncertainty, a grid independence study was performed over three meshes. Table 6 shows the details of these meshes. Table 7 compared the results at the probes listed in Table 4. The results from the medium mesh were the same as those in Table 5.

Table 5: Comparison of theoretical and Euler solutions for STI–1

	Theory			CFD		
	M	p, kPa	T, K	M	p, kPa	T, K
R	3.00	7.57	217	3.00	7.57	217
A	3.00	7.57	217	3.00	7.57	217
B	2.73	11.4	244	2.72	11.4	245
C	2.73	11.4	244	2.73	11.4	244
D	2.17	27.3	313	2.16	27.3	314
E	2.17	27.3	313	2.16	27.2	314
F	1.30	85.9	453	1.28	85.9	458
G	1.30	85.9	453	1.29	86.3	455
H	1.20	98.1	471	1.20	97.8	472
I	1.20	98.1	471	1.20	97.7	472

Table 6: Mesh details for STI–1

	Coarse	Medium	Fine
Average Grid Point Spacing	5 (10^{-3})	5 (10^{-4})	5 (10^{-5})
Cells	839 379	962 874	1 322 156
Faces	1 262 147	1 451 602	2 002 823
Nodes	422 769	488 729	680 668

Table 7: Comparison of solutions for each mesh, STI–1

	Coarse			Medium			Fine		
	M	p, kPa	T, K	M	p, kPa	T, K	M	p, kPa	T, K
R	3.00	7.57	217	3.00	7.57	217	3.00	7.57	217
A	3.00	7.57	217	3.00	7.57	217	3.00	7.57	217
B	2.72	11.4	245	2.72	11.4	245	2.73	11.4	244
C	2.73	11.4	244	2.73	11.4	244	2.72	11.4	245
D	2.17	27.2	314	2.16	27.3	314	2.17	27.2	313
E	2.17	27.2	314	2.16	27.2	314	2.17	27.2	314
F	1.30	86.0	455	1.28	85.9	458	1.30	85.5	454
G	1.30	86.2	454	1.29	86.3	455	1.29	86.1	456
H	1.20	97.3	471	1.20	97.8	472	1.20	97.5	471
I	1.20	98.2	471	1.20	97.7	472	1.19	98.5	473

Figure 18 shows the Mach number distribution along the STI centerline. The solutions for

each mesh had good agreement. Figures 19 shows the Mach number and static pressure contours for the design case STI–1 (medium mesh). The Euler model had overall good agreement with the theoretical solution but had shown to consistently overestimate the total pressure recovery by a slight margin. The total pressure recoveries were found to be 0.854, 0.854, and 0.860 for the coarse, medium, and fine meshes, respectively. The maximum difference from the theoretical solution ($\pi = 0.849$) was 1.3 percent.
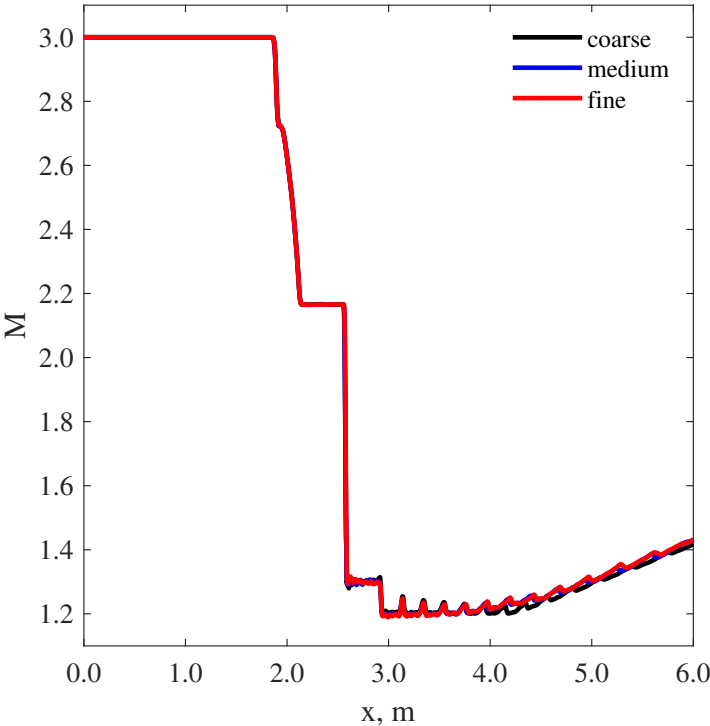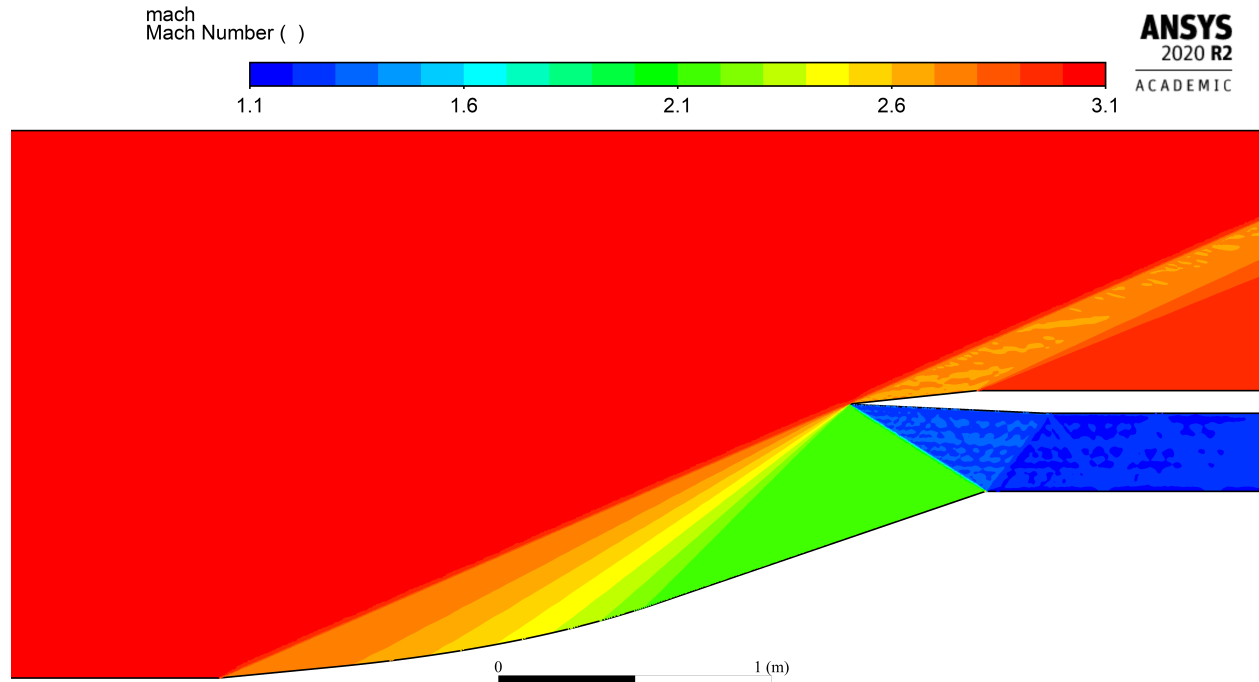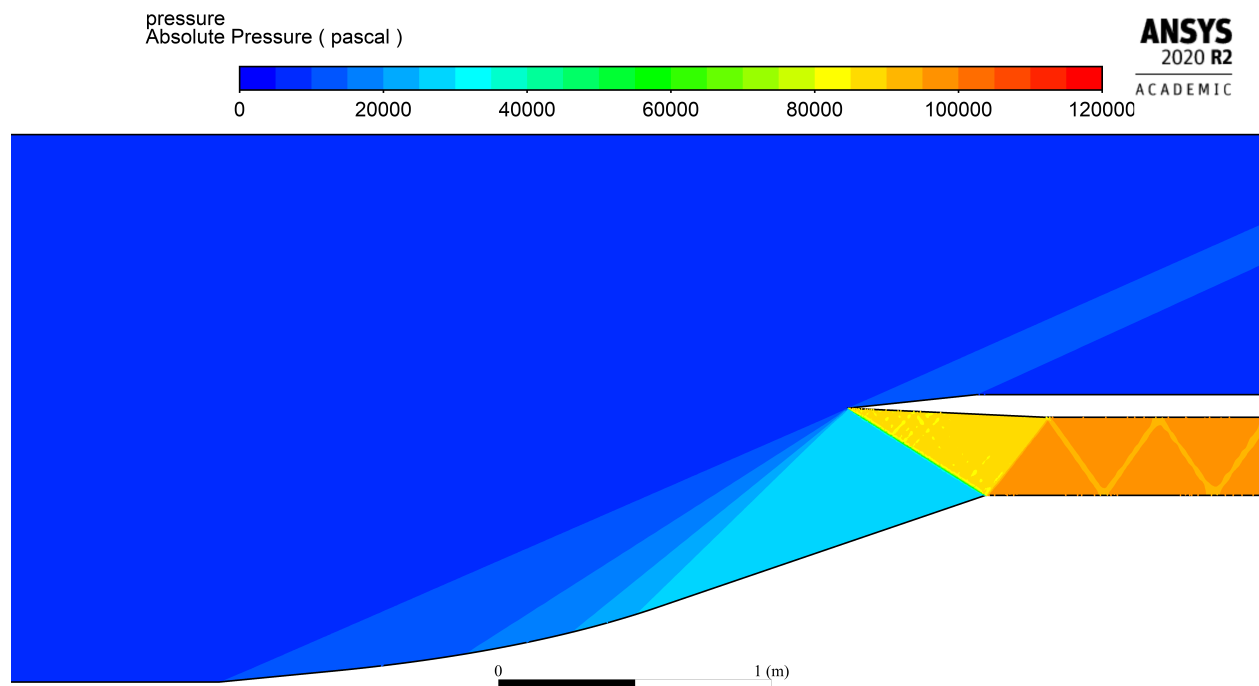

Figure 18: Centerline Mach number distribution for STI–1

(a) Mach number contours

(b) Static pressure contours

Figure 19: Design case STI–1 contours

38

3.5.2 Off-Design Conditions

At Mach numbers other than the design, or critical, Mach number of 3.0, the initial oblique shock and isentropic compression waves will miss the focus of the design flowfield. At subcritical speeds, the waves will intersect upstream of the cowl and allow flow spillage adding to drag. At supercritical speeds, the waves will intersect below the cowl and coalesce into a stronger oblique shock. This shock will miss the cowl tip and reflect through the internal duct instead of being canceled at the exit of the inlet. The STI was analyzed for the freestream Mach numbers between 2.9 and 3.4. Mach 3.4 was chosen to be the upper limit to prevent the total temperature, which does not change across a shock wave, from exceeding the lower limits of the autoignition temperature range for the fuels to be used in the RDE: hydrogen and propane. According to Conti and Hertzberg, the lower limit of the autoignition temperature for hydrogen is 773 K [76]. According to Bounaceur et al., the lower limit of the autoignition temperature for propane is 739 K [77]. Therefore, the propane autoignition temperature was the limiting value. Table 8 shows the off-design performance of STI–1. For comparison, the performance of the design case and the minimum total pressure recovery were also included in bold text.

Table 8: STI–1 Off-Design Performance

M_∞	$p_{t,\infty}$, kPa	$p_{t,\omega}$, kPa	$T_{t,\infty}$, K	π	π_{min}
2.9	239	164	582	0.687	0.822
3.0	**278**	**236**	**608**	**0.849**	**0.809**
3.1	323	262	634	0.812	0.769
3.2	374	296	661	0.791	0.783
3.3	433	338	690	0.782	0.769
3.4	501	390	719	0.778	0.756

Figure 20 plots the total pressure recovery at different freestream Mach numbers. As was expected, the design case had the highest performance. The supercritcal cases were lower performing and fell close to the minimum total pressure recovery line. The case with a freestream Mach number of 3.2 had the smallest margin of passing above the minimum

acceptable value among the supercritcal cases. The subcritical case fell far below the minimum total pressure recovery. This was because the STI was not started at this speed. It is expected that STI–1 will have difficulty starting below Mach 3; a behavior that was similar to other supersonic inlets incorporating isentropic compression, that is, Busemann inlets [19–21, 78].
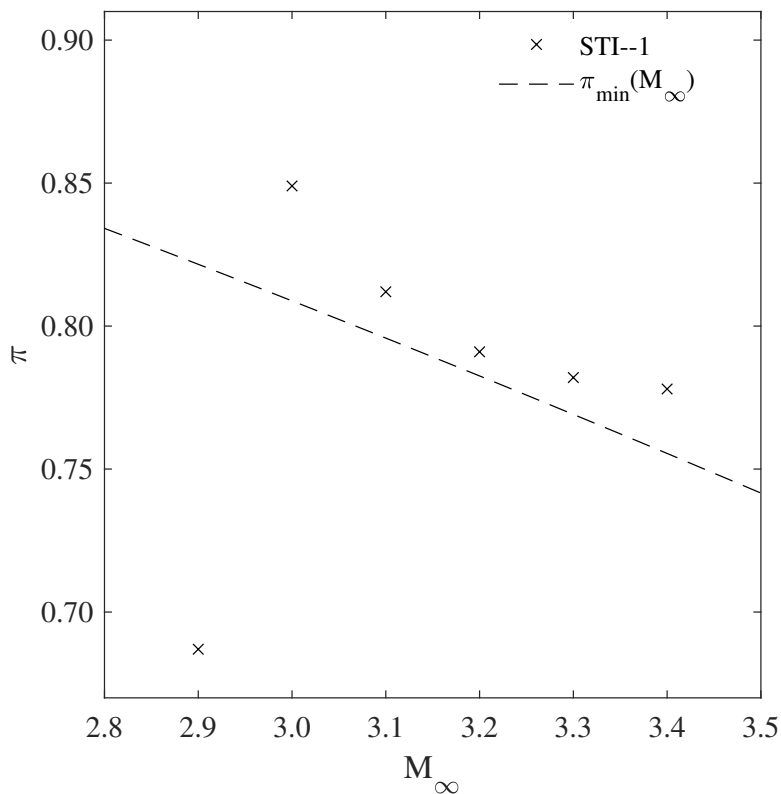
Figure 20: Total pressure recovery for STI–1

Figures 21 shows selected off-design Mach number contours. For the subcritical cases, the inlet was unstarted in Figure 21a, and the leading oblique shock and isentropic compression waves coalesced into a stronger oblique shock that reflected through the internal duct. In the supercritical cases, the flow expanded as it turned around the inlet shoulder and cowl.

(a) $M_\infty = 2.9$

(b) $M_\infty = 3.1$

(c) $M_\infty = 3.2$

(d) $M_\infty = 3.3$

(e) $M_\infty = 3.4$
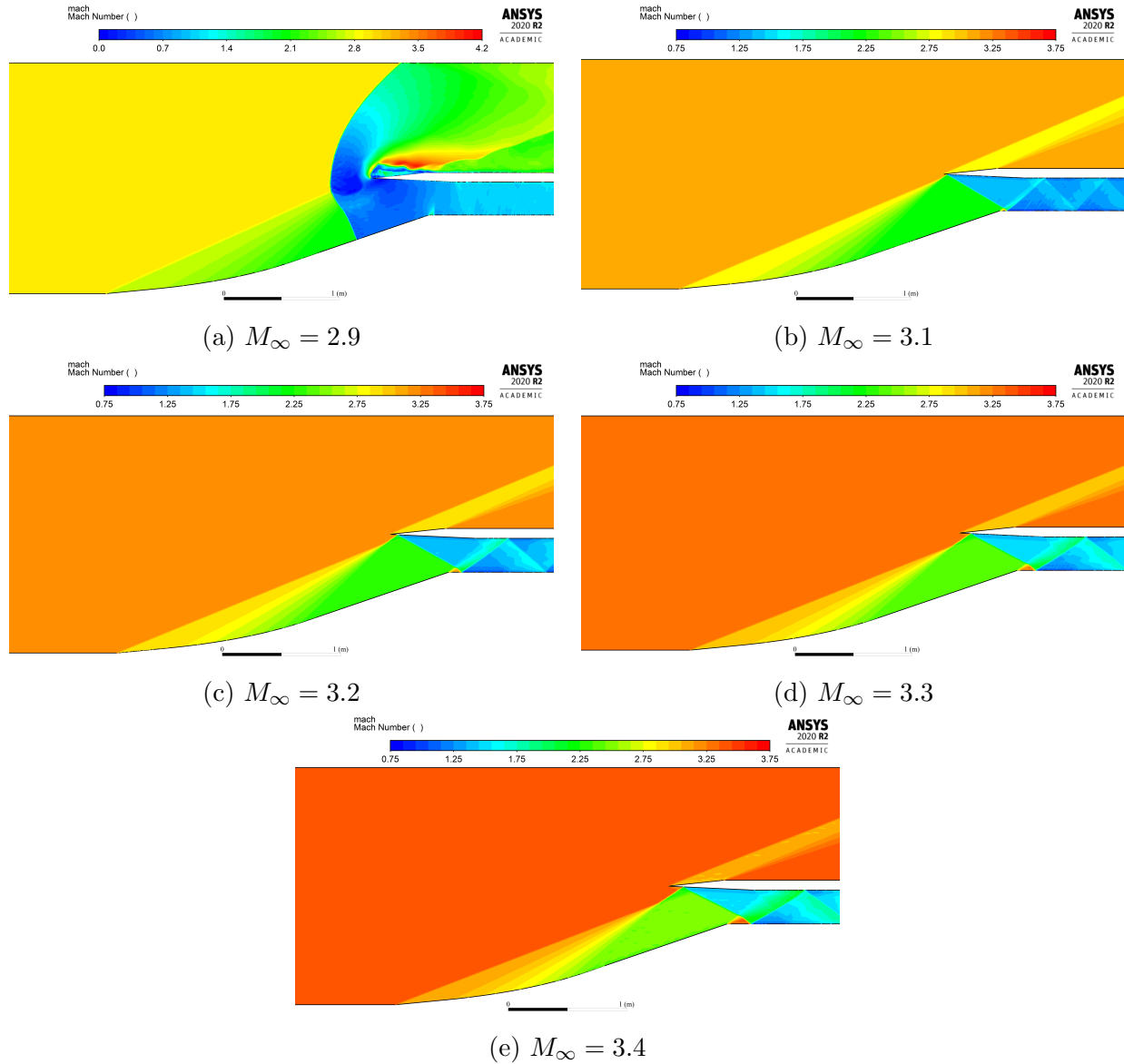
Figure 21: Off-design Mach number contours for STI–1

3.6 Performance of STI–2

3.6.1 On-Design Conditions

STI–2 utilized the symmetrical internal compression system. The parametric sweep as described in §3.4 was performed generating candidate STIs of varying performance. The gradient ascent optimization was applied to the candidate inlets to find the optimal balance of total pressure recovery and volumetric efficiency. Table 9 shows the maximum performance

candidates for the total pressure recovery, volumetric efficiency, and the optimum candidate for the specified design case. The optimum design from Table 9 can be seen in Figure 22. This design had been adopted as STI–2. Table 10 lists the flow direction from the freestream to the exit plane for STI–2 at the labeled points in Figure 22.

Table 9: Inlet candidates for STI–2

	θ_1, deg	M_3	π	$\eta_{\mathbb{V}}$	l/y_c
π_{max}	4.0	1.70	0.919	0.114	3.33
$\eta_{\mathbb{V},max}$	11.0	1.30	0.839	0.137	2.56
Optimum	8.7	1.62	0.898	0.127	3.01
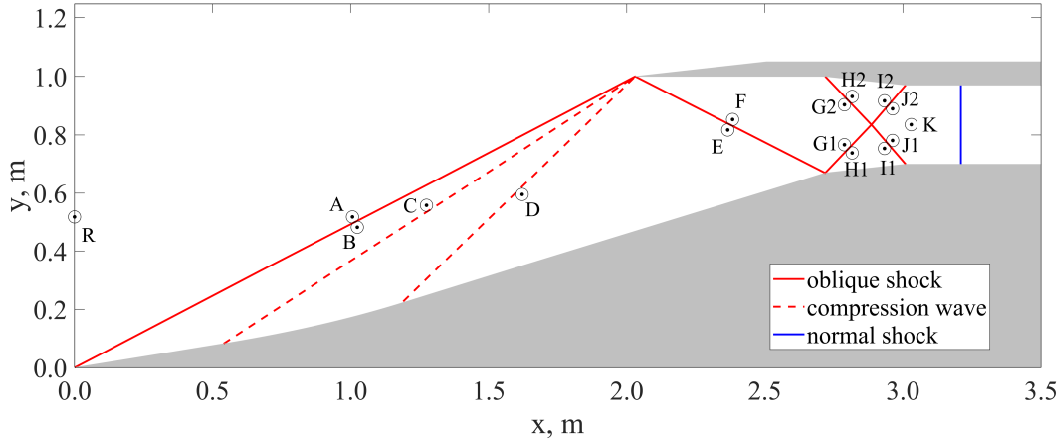
Figure 22: Schematic of STI–2 with associated shock structures

Table 10: STI–2 flow direction

Region	R–A	B–C	D–E	F–G1, G2	H1, H2–I1, I2	J1, J2–K
θ, deg	0.00	8.70	16.30	0.00	± 5.83	0.00

The mesh for STI–2 was made in Cadence Pointwise® where the boundary conditions were set as shown in Figure 23. The on-design case was performed in ANSYS Fluent® to verify that results consistent with the theoretical solution were attained. This was done to verify that the Euler model was correctly prepared to perform off-design analysis. Table 11 lists points upstream and within the STI where flow properties determined by the Euler

42

model were compared to the theoretical solution. The listed points were offset 2.0 cm from the theoretical shock structures so that the points would be well within the uniform region but far enough away from the shock structure to avoid any possible smearing of the shock in the analysis. Ultimately, the distance from the shock structure was arbitrary. Points were set on both sides of each shock wave. Points were also set upstream and downstream of the isentropic compression region. Note, point "R" was set in the freestream upstream of point "A" to verify that no issues arose in the freestream. These points can be seen in Figure 22. Table 12 shows the theoretical and Euler solutions to for the local Mach number, static pressure, and static temperature throughout STI–2. The percent difference between the theoretical and Euler solutions fell below one percent. For the Euler model, the total pressure recovery was found to be 0.900. This was a percent difference from the theoretical solution ($\pi = 0.898$) of less than one percent.
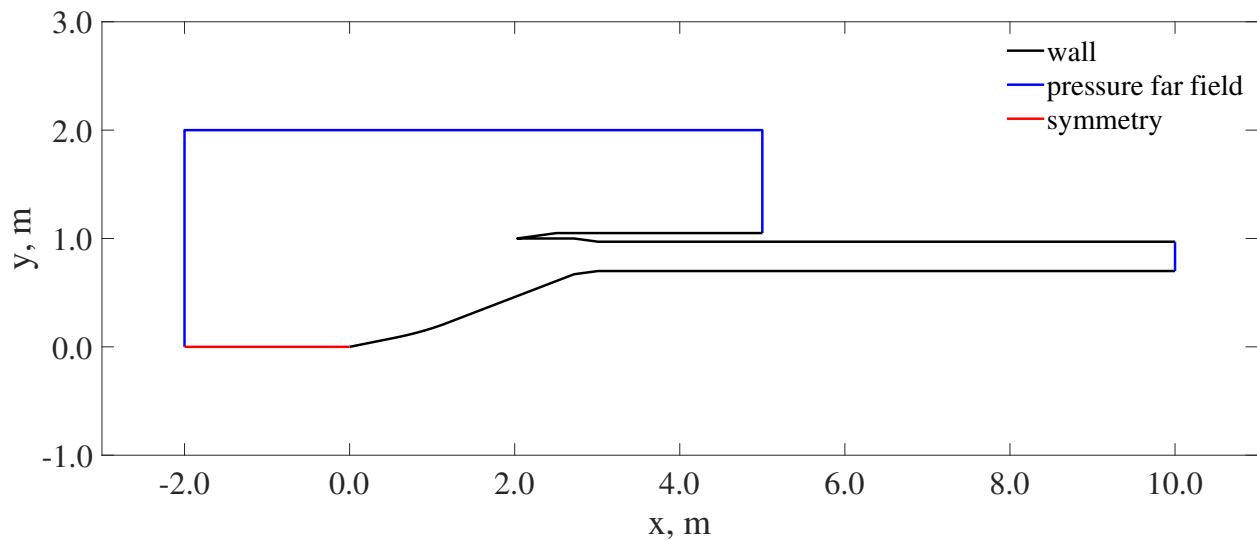

Figure 23: Boundary conditions and the domain extents of STI–2

Table 11: Locations of flow property monitors for STI #2

Station	x	y	Location description
R	0.00	0.52	Reference location upstream of Station "A"
A	1.01	0.52	Freestream condition; upstream of the initial oblique shock wave
B	1.02	0.48	Downstream of the initial oblique shock wave
C	1.28	0.56	Upstream of the isentropic compression region
D	1.62	0.60	Downstream of the isentropic compression region
E	2.37	0.82	Upstream of shock separating the external and internal compression systems
F	2.38	0.85	Downstream of shock separating the external and internal compression systems
G1	2.79	0.77	Upstream of symmetrical internal compression; lower location
G2	2.79	0.90	Upstream of symmetrical internal compression; upper location
H1	2.82	0.74	Downstream of first oblique shock in the symmetrical internal compression; lower location
H2	2.82	0.93	Downstream of first oblique shock in the symmetrical internal compression; upper location
I1	2.93	0.75	Upstream of second oblique shock in the symmetrical internal compression; lower location
I2	2.93	0.92	Upstream of second oblique shock in the symmetrical internal compression; upper location
J1	2.93	0.78	Downstream of symmetrical internal compression; lower location
J2	2.93	0.89	Downstream of symmetrical internal compression; upper location
K	3.03	0.84	Upstream of terminal normal shock

In addition to validating the Euler model through comparison with the theoretical solution, the Euler solution must also be verified to be independent of a specific mesh configuration. Three meshes for STI–2 of varying fineness were used to validate that the solution attained from the Euler model was independent of the mesh. Table 13 shows the details of the three meshes. The flow monitor locations from Table 11 were used to compare the results for the three meshes. Table 14 shows the results for each mesh. Note, the results for the medium mesh were the same results seen in §3.6.1.

44

Table 12: Comparison of theoretical and Euler solutions for STI–2

	Theory			Euler		
	M	p, kPa	T, K	M	p, kPa	T, K
R	3.00	7.57	217	3.00	7.57	217
A	3.00	7.57	217	3.00	7.57	217
B	2.57	14.3	262	2.57	14.2	262
C	2.57	14.3	262	2.57	14.3	262
D	2.25	23.3	302	2.25	23.4	302
E	2.25	23.3	302	2.26	23.3	301
F	1.62	57.8	400	1.61	58.1	400
G1	1.62	57.8	400	1.62	57.7	399
G2	1.62	57.8	400	1.62	57.8	399
H1	1.42	77.1	435	1.42	77.0	433
H2	1.42	77.1	435	1.42	77.1	434
I1	1.42	77.1	435	1.42	77.1	434
I2	1.42	77.1	435	1.41	77.1	434
J1	1.20	103	473	1.20	103	472
J2	1.20	103	473	1.19	104	473
K	1.20	103	473	1.21	103	471

Table 13: Mesh details for STI–2

	Coarse	Medium	Fine
Average Grid Point Spacing	$5\ (10^{-3})$	$5\ (10^{-4})$	$5\ (10^{-5})$
Cells	718 063	986 469	1 208 160
Faces	1 080 299	1 487 213	1 827 347
Nodes	362 237	500 745	619 188

Figure 24 shows the Mach number distribution along the centerline of the STI. The solutions for each mesh had good agreement. Therefore, the Euler model was determined to be independent of a specific mesh. The total pressure recoveries were found to be 0.898, 0.900, and 0.912 for the coarse, medium, and fine meshes, respectively. From these results, there was a maximum difference from the theoretical solution ($\pi = 0.898$) of 1.5 percent. The Euler model had overall good agreement with the theoretical solution but had shown to consistently overestimate the total pressure recovery slightly. Design case Mach number and

static pressure contours for STI–2 can be seen in Figures 25.

Table 14: Comparison of solutions for each mesh, STI–2

|	Coarse			Medium			Fine		
	M	p, kPa	T, K	M	p, kPa	T, K	M	p, kPa	T, K
R	3.00	7.57	217	3.00	7.57	217	3.00	7.57	217
A	3.00	7.57	217	3.00	7.57	217	3.00	7.57	217
B	2.57	14.2	262	2.57	14.2	262	2.57	14.2	262
C	2.57	14.2	262	2.57	14.3	262	2.57	14.2	262
D	2.25	23.3	302	2.25	23.4	302	2.25	23.3	302
E	2.25	23.3	302	2.26	23.3	301	2.25	23.3	301
F	1.61	57.8	401	1.61	58.1	400	1.62	57.6	398
G1	1.61	58.0	400	1.62	57.7	399	1.61	57.8	400
G2	1.62	57.6	399	1.62	57.8	399	1.61	57.9	399
H1	1.41	77.4	435	1.42	77.0	433	1.41	77.0	434
H2	1.41	77.3	434	1.42	77.1	434	1.41	77.1	434
I1	1.41	77.3	435	1.42	77.1	434	1.41	77.1	434
I2	1.42	76.9	433	1.41	77.1	434	1.41	77.1	434
J1	1.20	103	472	1.20	103	472	1.20	103	472
J2	1.20	103	472	1.19	104	473	1.20	103	472
K	1.20	103	472	1.21	103	471	1.20	103	472
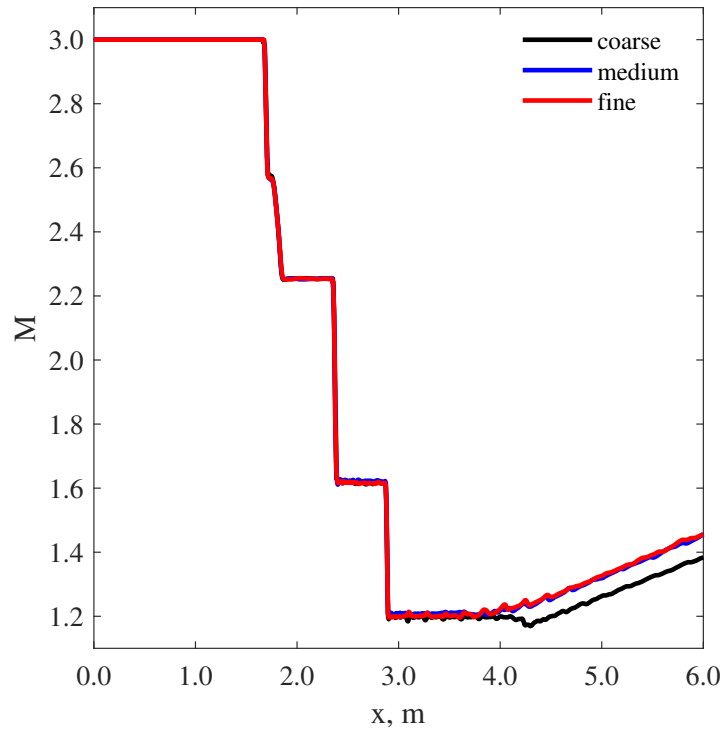
Figure 24: Centerline Mach number distribution for STI–2
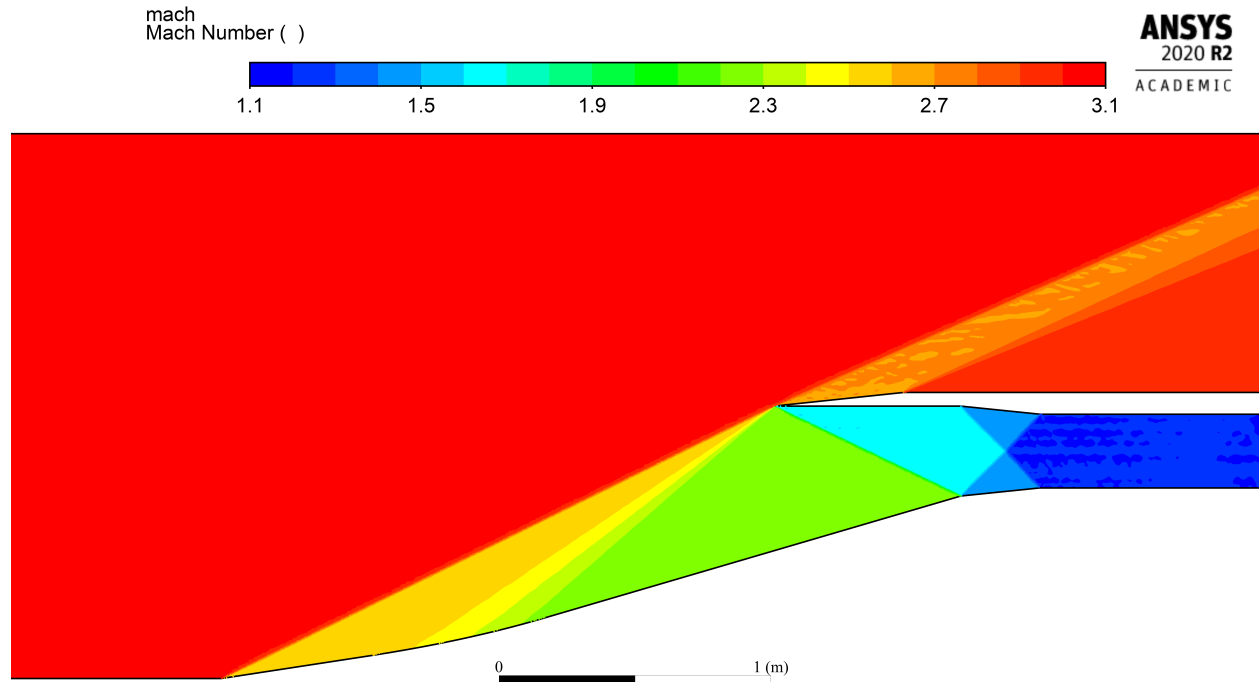
(a) Mach number contours
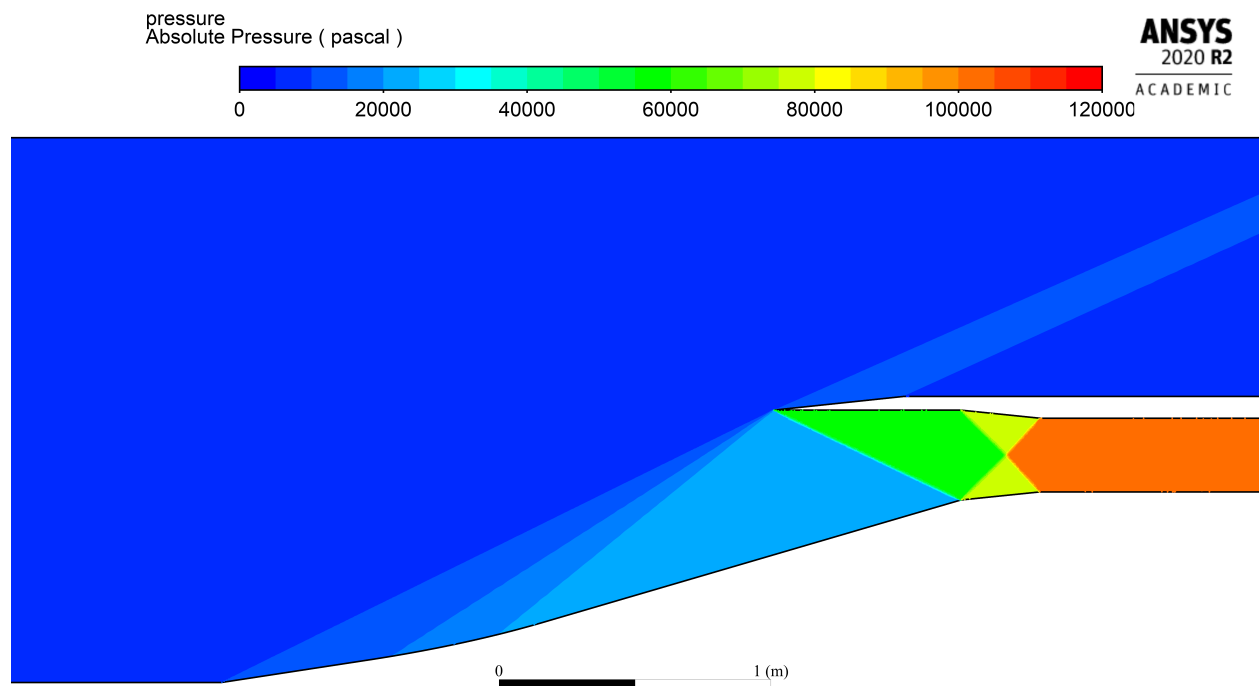
(b) Static pressure contours

Figure 25: Design case STI–2 contours

3.6.2 Off-Design Conditions

At Mach numbers other than the design, or critical, Mach number $M_\infty = 3$, the initial oblique shock and isentropic compression waves will miss the focus of the design flowfield. At subcritical speeds, the waves will intersect upstream of the cowl and allow flow spillage adding to drag. At supercritical speeds, the waves will intersect below the cowl and coalesce into a stronger oblique shock. This shock will miss the cowl tip and reflect through the STI internal duct instead of being cancelled at the exit of the inlet. The STI was analyzed from freestream Mach numbers 2.9 to 3.4. Mach 3.4 was chosen to be the upper limit to prevent the total temperature, which does not change across a shock wave, from exceeding the lower limits of the autoignition temperature range for the fuels to be used in the RDE: hydrogen and propane. According to Conti and Hertzberg, the lower limit of the autoignition temperature for hydrogen was 773 K [76]. According to Bounaceur et al, the lower limit of the autoignition temperature for propane was 739 K [77]. Therefore, the propane autoignition temperature was the limiting value. Table 15 shows the off design performance of STI–2. For comparison, the design case and minimum total pressure recovery were also included in bold text.

Table 15: STI–2 Off-Design Performance

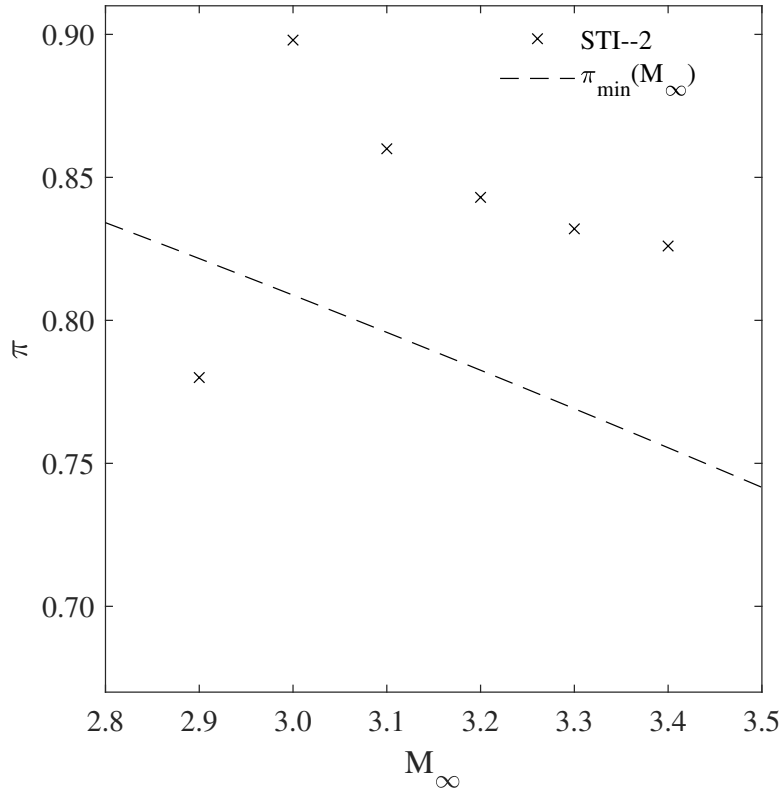| M_∞	$p_{t,\infty}$, kPa	$p_{t,\omega}$, kPa	$T_{t,\infty}$, K	π	π_{min}
2.9	239	187	582	0.780	0.822
3.0	**278**	**246**	**608**	**0.898**	**0.809**
3.1	323	278	634	0.860	0.796
3.2	374	315	661	0.843	0.783
3.3	433	360	690	0.832	0.769
3.4	501	413	719	0.826	0.756

Figure 26: Total pressure recovery for STI–2

The total pressure recovery was plotted against the freestream Mach number in Figure 26. As was expected, the design case was the highest performing case. The incoming flow with a freestream Mach number of 3.2 hads the smallest margin of passing above the minimum acceptable value among the supercritcal cases. The subcritical case fell below the minimum below the minimum total pressure recovery. The subcritical operation of STI–2 had a normal shock standing in the inlet. The total pressure drop across the shock accounted for the low total pressure recovery at Mach 2.9. Off design Mach number contours can be seen in Figures 27. As mentioned previously for STI–1, the initial oblique shock and isentropic compression waves coalesced into a stronger oblique shock and reflected through the internal duct. In the supercritical cases, the flow expanded as it turns around the inlet shoulder.
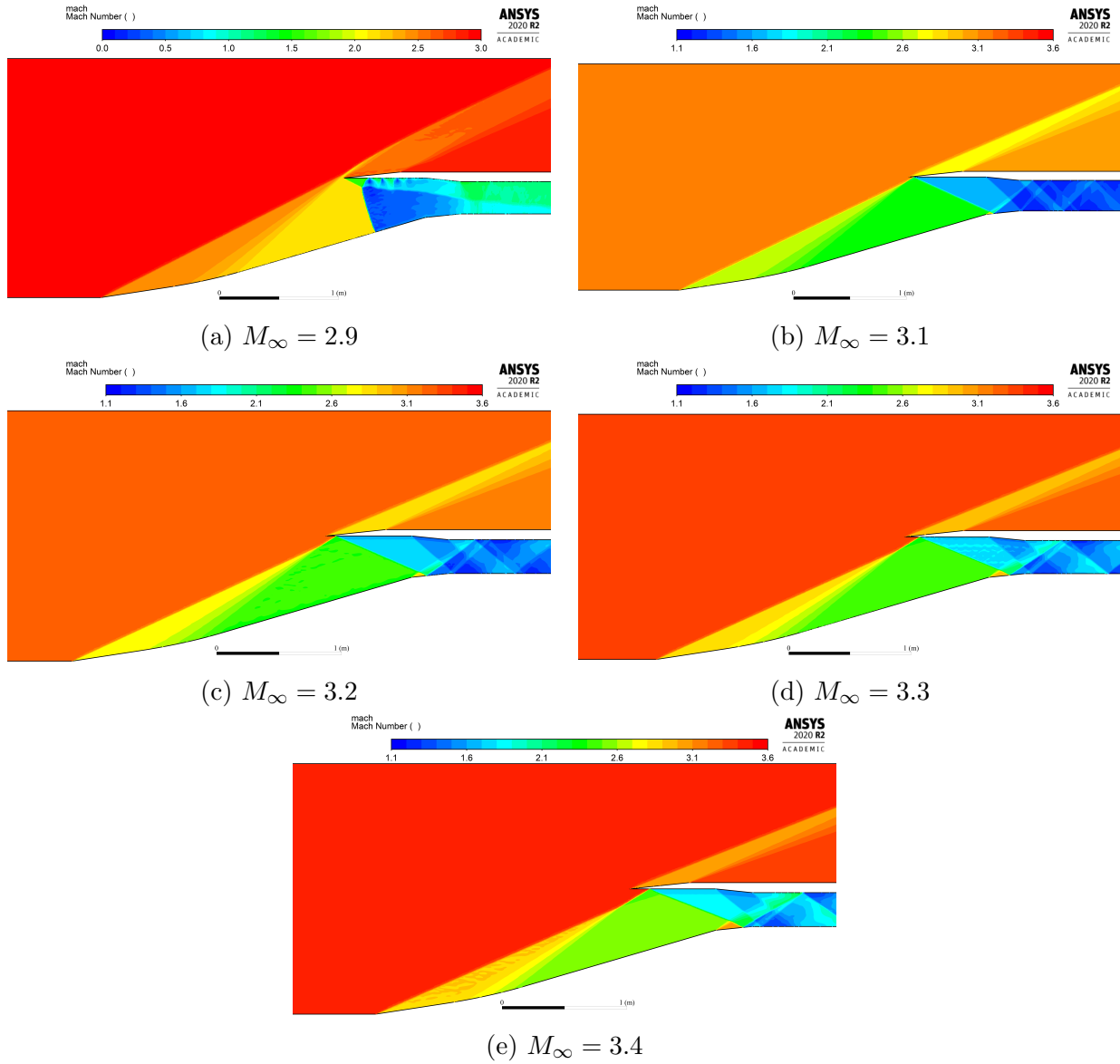
(a) $M_\infty = 2.9$

(b) $M_\infty = 3.1$

(c) $M_\infty = 3.2$

(d) $M_\infty = 3.3$

(e) $M_\infty = 3.4$

Figure 27: Off-design Mach number contours for STI–2

3.7　Conclusion

Table 16 collects the STI performance from Sections 3.5 and 3.6.

Table 16: Summary of STI Performance

| M_∞ | $P_{t,\infty}$, kPa | $T_{t,\infty}$ | STI–1 | | STI–2 | | |
			$P_{t,\omega}$, kPa	π	$P_{t,\omega}$, kPa	π	π_{min}
2.9	239	582	164	0.687	187	0.780	0.822
3.0	278	608	236	0.849	246	0.898	0.809
3.1	323	634	262	0.812	278	0.860	0.796
3.2	374	661	296	0.791	315	0.843	0.783
3.3	433	690	338	0.782	360	0.832	0.769
3.4	501	719	390	0.778	413	0.826	0.756

Recall that the volumetric efficiency $\eta_\mathbb{V}$ was 0.123 for STI–1 and 0.127 for STI–2. The length per capture height l/y_c was 3.02 for STI–1 and 3.01 for STI–2. Figure 28 compares the total pressure recovery of the two STIs.
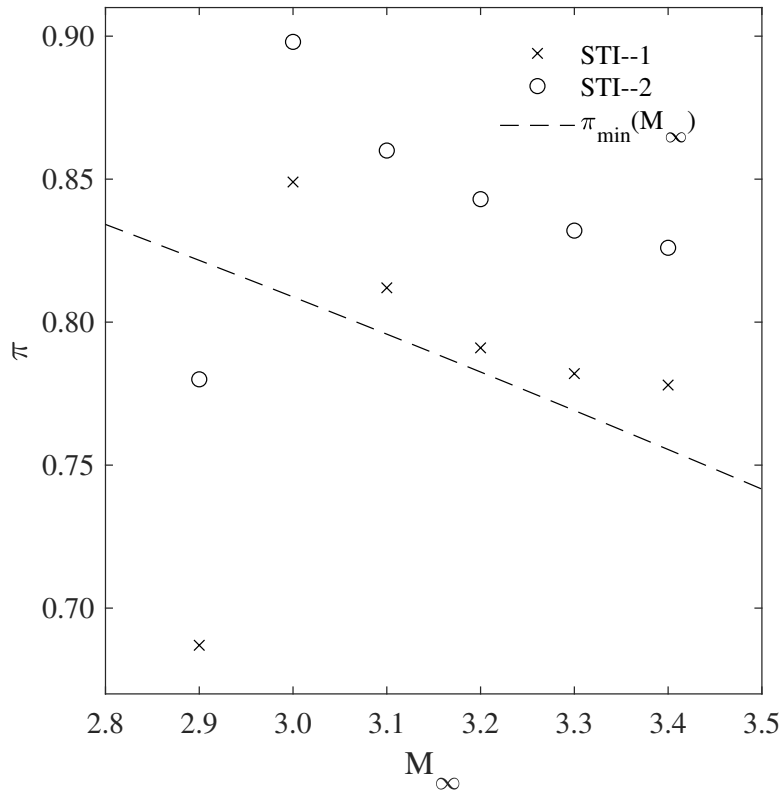

Figure 28: Total pressure recovery for STI–1 and STI–2

Overall, STI–2 outperformed STI–1 in the performance categories. The performance differences were marginal in the volumetric efficiency and length, but significant in the total pressure recovery. The ability of STI–2 to perform at a wider range of flight Mach number was another boon for the second design. If a choice must be made between the two designs, STI–2 was the better choice.

Mizener et al. [58] designed a set of waverider forebodies based on the two-dimensional osculating flowfield at the freestream Mach number of 3.0. Their process led to the development of two models comparable to the STI in the present work. For Mizener et al.'s forebody Models #1 and #2, they reported total pressure recoveries of approximately 0.72 and approximately 0.88, respectively. These values represented the best performing inlets for their parametric sweeps. Mizener et al. [58] reported the volumetric efficiency for only their Model #2. They reported the highest volumetric efficiency for a range of osculating cone angle of 5–8 deg as $\eta_{\mathbb{V}} = 0.0623$–$0.0807$. Compared to Mizener et al.'s Model #1 at $M_{\infty} = 3.0$, STI–1's volumetric efficiency exceeded it by approximately 0.13. Compared to Mizener et al.'s Model #2 at $M_{\infty} = 3.0$, STI–2's total pressure recovery was slightly greater by approximately 0.02 and had a greater volumetric efficiency by approximately 4.6–6.5 percent.

4 Integration of STI and RDE

4.1 RDE Model

The present work uses the control volume analysis for RDEs developed by Mizener and Lu [50,51]. Figure 29 shows a diagram of the control volume defined as an annulus composing of the injection plane, the exit plane, and two co-annular cylindrical walls. The model considers only a straight annulus with no variation in cross-sectional area or nozzle. It is fixed in space, and the flow inside it is assumed to be inviscid, cyclical, and with no body forces. Property variations in the radial direction are neglected. Potential losses such as incomplete fuel/oxidizer mixing and contact burning along the slipline are also neglected.
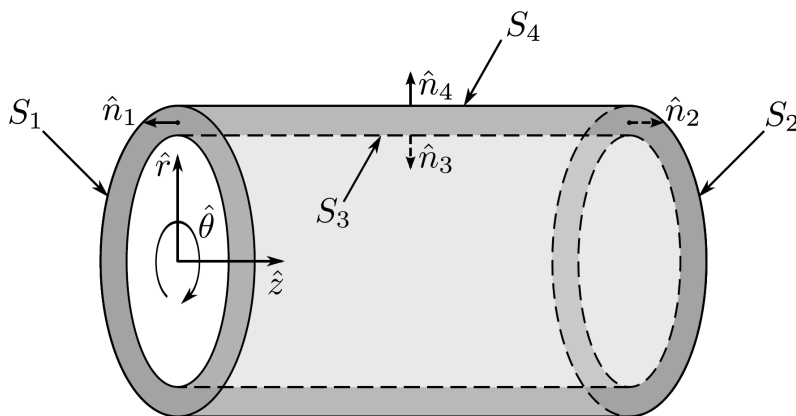

Figure 29: Diagram of the STI model control volume from [51]

A thorough description of the injector conditions and internal flow of the RDE model is provided by Mizener and Lu [50] and Mizener [51]. A brief overview can suffice here. The properties of gas mixtures of unburned fuel and oxidizer are calculated from the *CRC Handbook of Chemistry and Physics* [79, 80] and the 1976 U.S. Standard Atmosphere [70]. Cantera [81] and the California Institute of Technology's Shock and Detonation Toolbox [82] are used to calculate detonation properties, assuming choked flow upstream of the detonation wave and equilibrium conditions.

Figure 30 illustrates the major features of the internal flow model within the RDE an-

nulus. The boundary conditions of the internal flow model are informed by the injector conditions at the injection plane of the annulus. The unrolled RDE annulus in Figure 30 is divided into three circumferential regions where each injector condition influenced the internal flow downstream of the annulus injection plane. The injection modes are no injection (region "A"), subsonic injection (region "B"), and sonic injection (region "C").
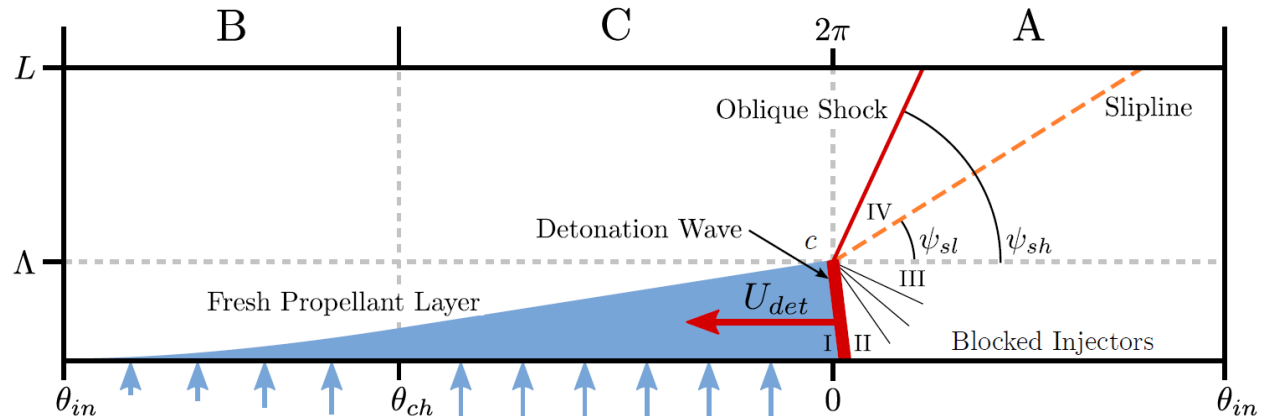

Figure 30: Diagram of an unrolled RDE annulus [51]

Four internal flow regions (region I upstream of the detonation wave, region II downstream of the detonation wave and upstream of the flow expansion, region III downstream of the flow expansion and slipline and upstream of the oblique shock, and region IV downstream of the oblique shock bounded by the slipline) are distinguished by the detonation and shock structures within the RDE annulus. The internal flow model determines the state of these regions in three steps: determination of the shock and slip-line angles, flow expansion and detonation wave height, and exit flow angles and shock wave turning. The first step handles the determination of the angle of the contact surface between the product gases of the detonation wave with the product gases of a previous pass of the detonation wave and the angle of the oblique shock attached to the detonation wave. The second step handles the determination of the expansion area behind the detonation wave and the detonation wave height. The third step handles the determination of the exit flow angles and shock wave turning of the oblique shock and slipline. It has been observed that a portion of the

flow recirculated and is turned by the oblique shock [83, 84]. The turning angle of the flow by this shock is also determined in the third section. The mass, energy, and momentum conservation equations are integrated over the control volume.

4.2 STI/RDE Integration Method

The STI/RDE integration is examined using the low-order parametric RDE model and code developed in Mizener [50, 51]. Since the duct between the exit plane of the supersonic inlet and the RDE plenum are neglected in the code, the performance of the STI and the RDE are calculated separately in the current work. The exit conditions from the STI are taken to be the RDE plenum conditions. Two types of fuels, hydrogen and propane, are considered, with air as the oxidizer. It is assumed: 1) a given fuel will ignite if the total temperature of the air entering the RDE is above the fuel's auto-ignition temperature, and 2) the equivalence ratio of the fuel/air mixture is stoichiometric at the RDE entrance. The RDE code determines the engine performance for a parameterized annulus. The model sweeps through the engine length l from 15 to 50 cm for multiple annulus thicknesses δ_a: 1.0, 2.5, 5.0, 7.5, and 10.0 cm. A number of engine variables are held constant: the annulus outer diameter ($d_o = 30$ cm), the propellant injection angle with respect to the positive axial direction ($\psi_{inj} = 0$ deg), and the equivalence ratio ($\phi = 1$). The annulus inner diameter is determined by

$$d_i = d_o - 2\delta_a \tag{36}$$

In the waverider forebody/RDE integration study [58], it was found the RDE performance was only a function of the total pressure, not the inlet Mach number, velocity, or dynamic pressure. With the STI performance determined, the exit conditions are fed into the RDE to determine the integrated system performance.

4.3 Performance Metrics

The performance metrics of the integrated STI/RDE system are chosen to be the thrust F_z, resultant engine torque on the control volume τ, fuel-based specific impulse $(I_{sp})_f$, and thrust-specific fuel consumption TSFC. The thrust and fuel-based specific impulse are to be maximized, and the engine torque on the control volume and the thrust-specific fuel consumption are to be minimized.

The thrust is given by performing a momentum balance on the RDE control volume. The integral over the control volume is expressed as

$$F_z = \delta_a r_m \int_0^{2\pi} \left(\rho V_z^2 + p - p_\infty \right)_{out} d\theta - \rho_\infty V_\infty^2 A_{in} \tag{37}$$

The resultant engine torque on the control volume is determined by

$$\tau = r_m F_\theta \tag{38}$$

where the circumferential thrust is expressed by the integral

$$F_\theta = \delta_a r_m \int_0^{2\pi} \left(\rho V_\theta V_z \right)_{out} d\theta \tag{39}$$

Mizener and Lu noted that zero-torque operating points did exist and may prove useful in design optimization [50]. The fuel-based specific impulse is expressed as

$$(I_{sp})_f = \frac{\| F_z + F_\theta \|}{\dot{m}_f g_0} \tag{40}$$

The fuel-based specific impulse is chosen over the specific impulse calculated using the axial thrust and propellant flow rate $\dot{m}_{inj}$ to follow convention established in the literature [58,

60, 85–90]. The thrust specific fuel consumption is determined by

$$\text{TSFC} = \frac{\dot{m}_f}{F_z} \tag{41}$$

4.4 Results and Discussion

4.4.1 STI–1/RDE

For the integration of STI–1 and RDE, the engine performance was calculated for the RDEs sized in the parametric sweep. The STI exit total pressure $p_{t,\omega}$ and total temperature $T_{t,\infty}$ from Table 8 were input into the RDE model. During the parametric sweep of the annulus length (l =15 to 50 cm) it was found that he best engine performance occurred at an engine length of 15 cm. Cases where the solution failed to converge were for narrow annuli, namely, δ_a = 1.0 and 2.5 cm. In those cases, the engine with best performance was the shortest length that had a converged solution. This follows a similar conclusion by Mizener et al. [51,58]. Note, in the manner that the integrated model was setup, the engine performance was a function of the total pressure at the exit of the STI. While the STI performance was dependent on freestream Mach number, analytically, the RDE performance depended on the total pressure at the injection plane. In the figures presented, all performance values were plotted versus freestream Mach number to more easily relate the RDE performance to the STI, but a more direct (or rigorous) presentation should use the total pressure values for the RDE. In Figures 31–34, all data were presented for the minimum length of the engine $l = 15$ cm. It was shown that the cases where hydrogen was used resulted in more cases where the solution did not converge. Figure 31 shows that propane results in a slightly greater maximum thrust when compared to the hydrogen-fueled cases. Figure 32 shows that cases using hydrogen resulted in larger resultant torque values than cases using propane.
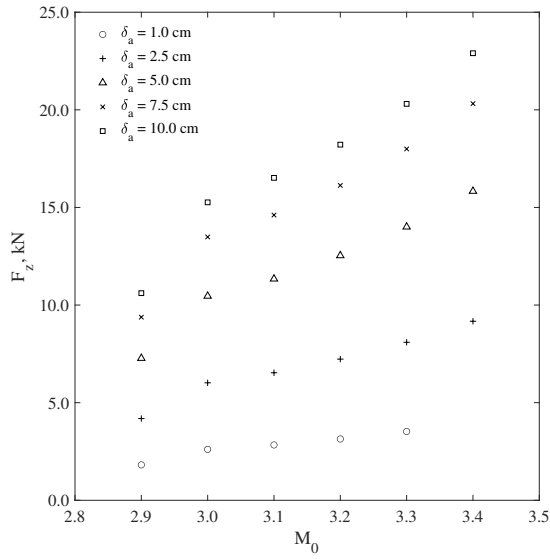
(a) Propane
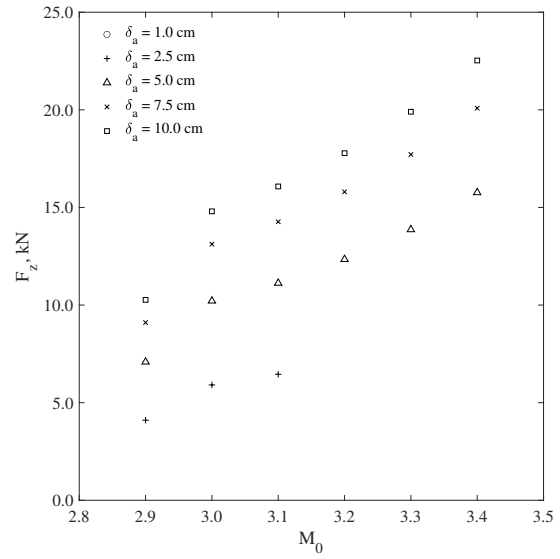
(b) Hydrogen

Figure 31: STI–1 integrated with parametric RDE performance, thrust F_z
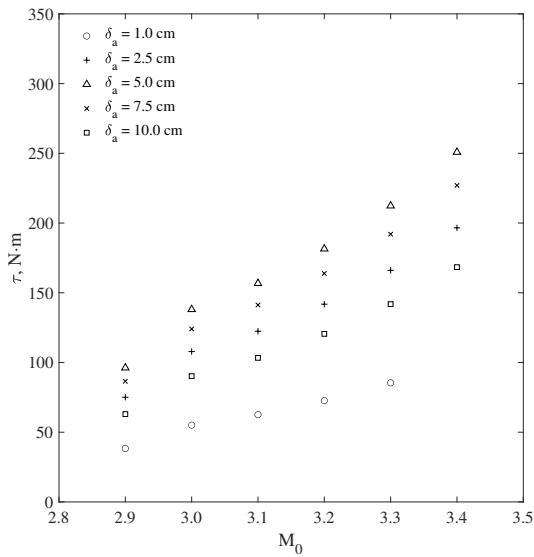
(a) Propane
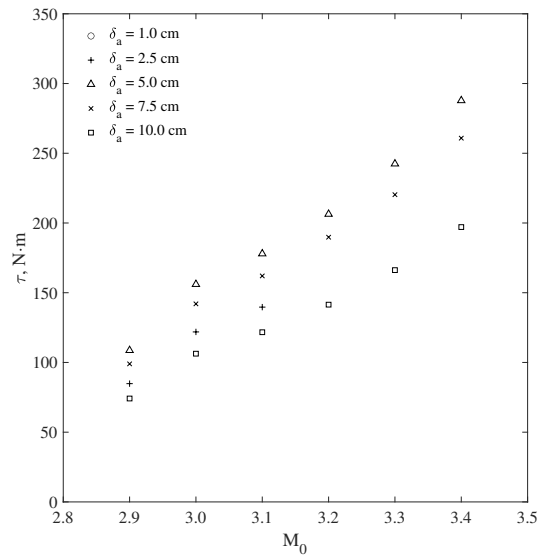
(b) Hydrogen

Figure 32: STI–1 integrated with parametric RDE performance, torque τ

In Figure 32, the maximum torque for the minimum length engines occurred for the annulus width of 5.0 cm. For the minimum length engine, the minimum torque occurred for $\delta_a = 1.0$ cm followed by $\delta_a = 10.0$ cm. Not shown in Figure 32, the minimum resultant torque within

the parametric sweep occurred at much longer engine lengths, near or at $l = 50$ cm. For cases using propane , the minimum torque was $\tau < 10$ N · m, and for cases using hydrogen, the minimum torque was $\tau < 25$ N · m. When it was found that three out of four of the performance metrics occurred at the minimum engine length, it was decided that the torque at the minimum engine length would be reported and optimization for minimum torque would be left to future studies.

The maximum fuel-based specific impulse occurred for the narrowest annulus that a converged solution exists. The $(I_{sp})_f$ of cases for hydrogen was approximately 2.3 times greater than that of the equivalent case for propane. As Mach number increases, there was not significant variation in $(I_{sp})_f$.

(a) Propane

(b) Hydrogen

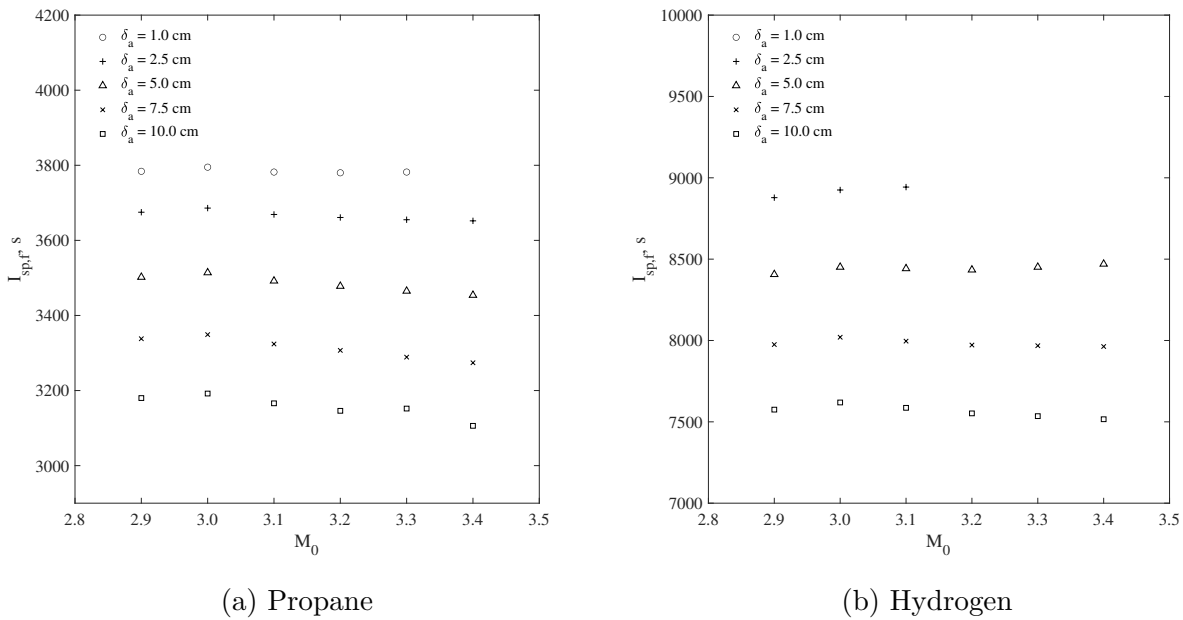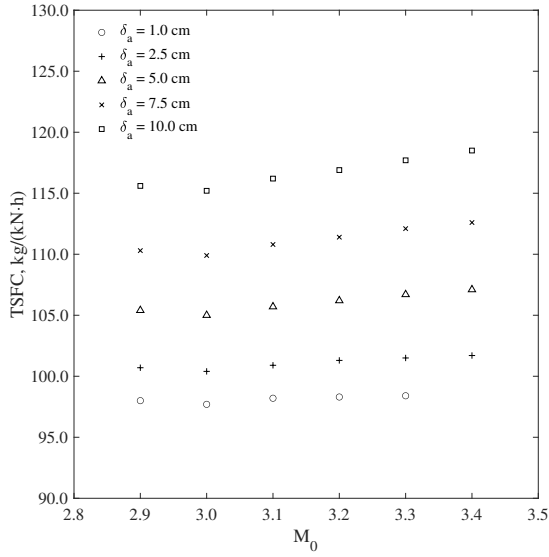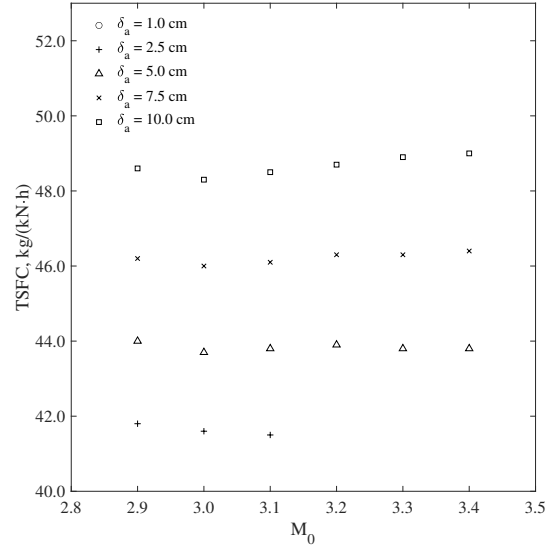Figure 33: STI–1 integrated with parametric RDE performance, fuel-based specific impulse $(I_{sp})_f$

(a) Propane   (b) Hydrogen

Figure 34: STI–1 integrated with parametric RDE performance, TSFC

The thrust-specific fuel consumption for the propane cases was approximately 2.3 to 2.4 times greater than that of the hydrogen cases. Similar to the $(I_{sp})_f$, there was not a large variation in TSFC as Mach number changes.

To reiterate, it was found that the highest performing RDEs were those of the shortest engine length within the parametric sweep; generally, $l = 15$ cm. Also, the performance metric of torque was abandoned as minimizing τ worked against the other three performance metrics. Table 17 shows the cases of highest performance for each metric.

Table 17: High performance cases for STI–1 integrated with RDE

Case	Fuel	M_∞	δ_a, cm	F_z, kN	τ, N·m	$(I_{sp})_f$, s	TSFC, kg/(kN·h)
Maximum F_z	propane	3.4	10.0	22.9	168	3 106	119
Maximum $(I_{sp})_f$	hydrogen	3.1	2.5	6.45	140	8 943	41.5
Minimum TSFC	hydrogen	3.1	2.5	6.45	140	8 943	41.5

Note, the maximum $(I_{sp})_f$ and minimum TSFC cases occurred for the same annulus length and width. Unless, one needed to prioritize thrust, it would seem to reason to select a hydrogen-fueled RDE of $l = 15$ cm, $\delta_a = 2.5$ cm. However, reviewing Figures 31–34 shows

60

that solutions failed to converge throughout the entire range of Mach numbers for $\delta_a = 2.5$ cm. If one increases the annular width to 5 cm, the resultant torque sharply increases. Let δ_a be increased to 10 cm. At this engine configuration, the $(I_{sp})_f$ and TSFC were comparatively worse than the maximum $(I_{sp})_f$/minimum TSFC case, but the $(I_{sp})_f$ and TSFC were still much better than the maximum F_z case. Therefore, for STI–1, an RDE with an annulus length of 15 cm and width of 10 cm was selected as the best performing integrated pair across the Mach range of 2.9 to 3.4. The RDE chosen follows the conclusion reached by Mizener et al. that a short and thick annulus exhibit better performance [58].

4.4.2 STI–2/RDE

For the RDE integration with STI–2, the STI exit total pressure $p_{t,\omega}$ and total temperature $T_{t,\infty}$ from Table 15 were input into the RDE model to calculate the engine performance data for a parametric engine size. In general, it was found that the best engine performance occurred at an engine length of 15 cm. Cases where the solution failed to converge were for narrow annuli, that is, $\delta_a = 1.0$ and 2.5 cm. In those cases, the engine with the best performance was the shortest annulus that had a converged solution. This follows the conclusion made by Mizener [51] and Mizener et al. [58]. Note, in the manner that the integrated model was setup, the engine performance was a function of the total pressure at the exit of the STI. While the STI performance was dependent on freestream Mach number, analytically the RDE performance was dependent on the total pressure in the plenum. In the figures presented, all performance values were plotted versus freestream Mach number to more easily relate the RDE performance to the STI, but a more direct (or rigorous) presentation should use the total pressure values for the RDE. In Figures 35–38, all data were presented for the minimum length of the engine $l = 15.0$ cm.
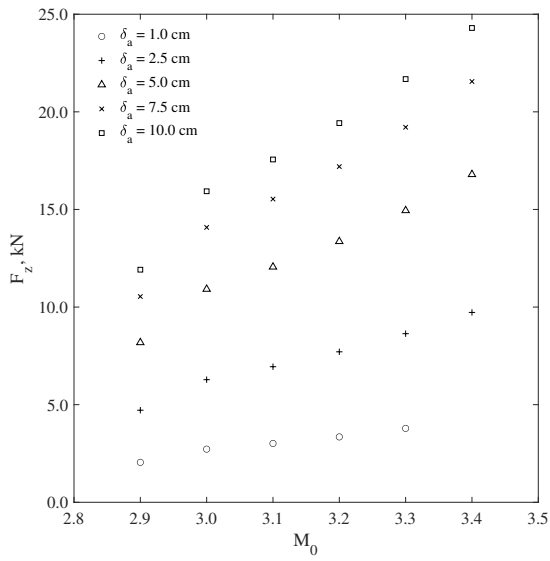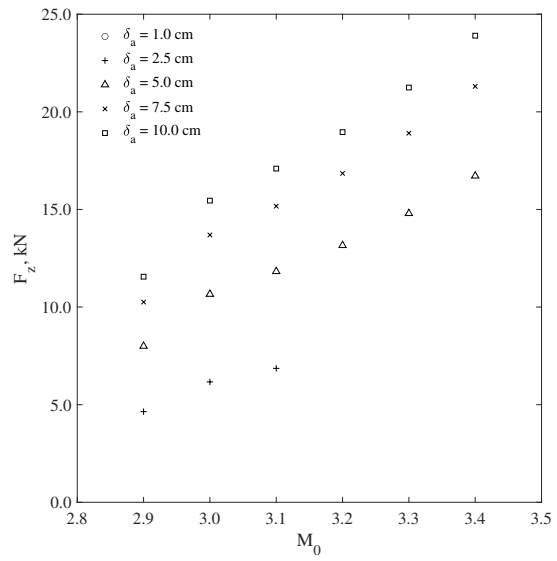
(a) Propane (b) Hydrogen

Figure 35: STI–2 integrated with parametric RDE performance, thrust F_z
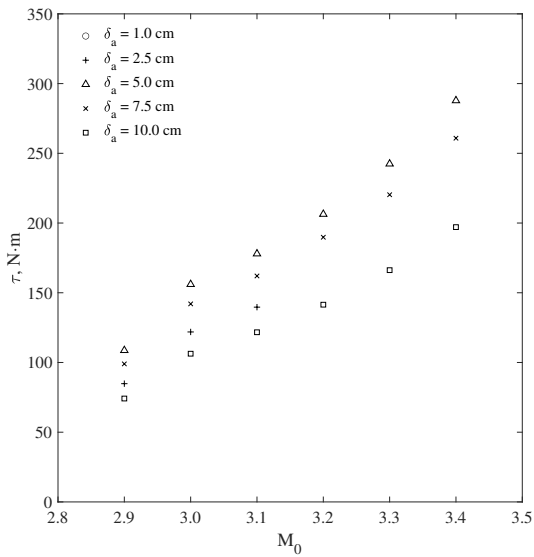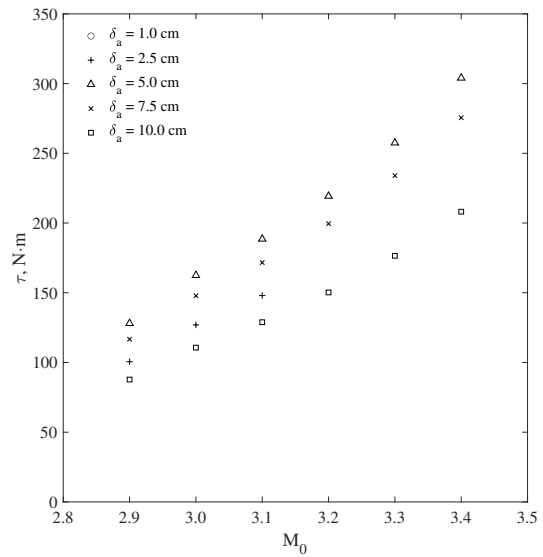
(a) Propane (b) Hydrogen

Figure 36: STI–2 integrated with parametric RDE performance, torque τ

More cases with hydrogen failed to converge. Figure 35 shows that propane results in a slightly greater maximum thrust when compared to hydrogen-fueled cases. Figure 36 shows that cases using hydrogen resulted in larger resultant torque values than cases using propane.

In Figure 36, the maximum torque for the minimum length engines occurred for the annulus width of 5 cm. For the minimum length engine, the minimum torque occurred for $\delta_a = 10$ cm. Not shown in Figure 36, the minimum resultant torque within the parametric sweep occurred at much longer engine lengths, near or at $l = 50$ cm. For cases using propane, the minimum torque was $\tau < 10$ N $\cdot$ m, and for cases using hydrogen, the minimum torque was $\tau < 25$ N $\cdot$ m. When it was found that three out of four of the performance metrics occurred at the minimum engine length, it was decided that the torque at the minimum engine length would be reported and optimization for minimum torque would be left to future studies.

The maximum fuel-based specific impulse occurred for the narrowest annulus for a converged solution exists. The $(I_{sp})_f$ of cases for hydrogen was approximately 2.3 times greater than that of the equivalent case for propane. There was not significant variation in $(I_{sp})_f$ with an increase in Mach number.

(a) Propane
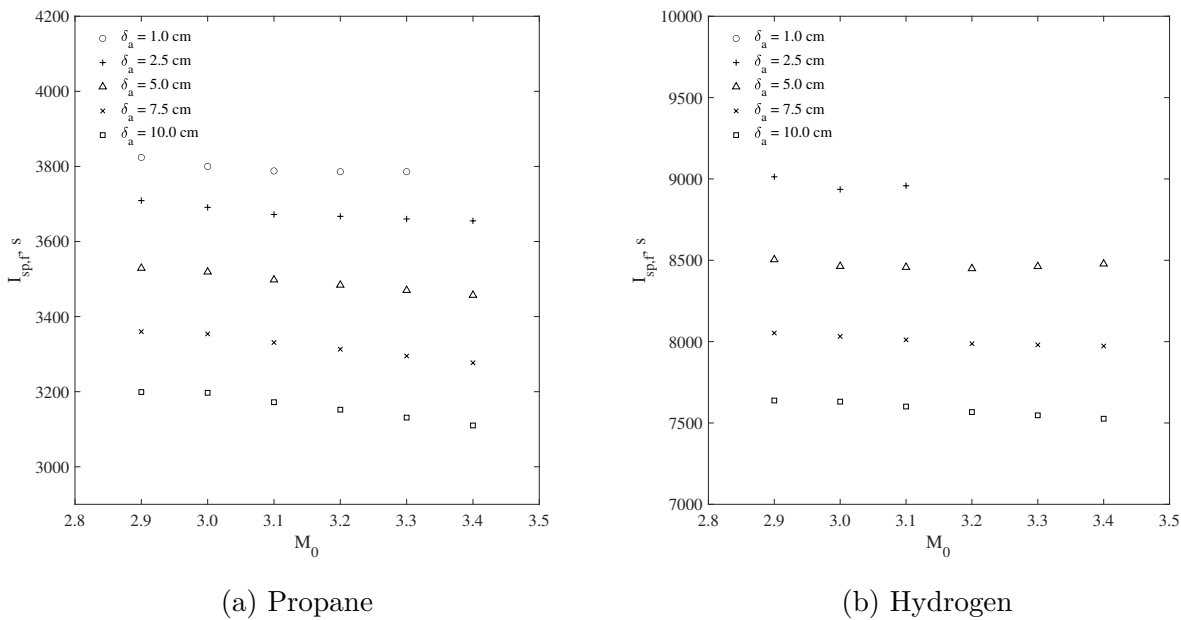
(b) Hydrogen

Figure 37: STI–2 integrated with parametric RDE performance, fuel-based specific impulse $(I_{sp})_f$
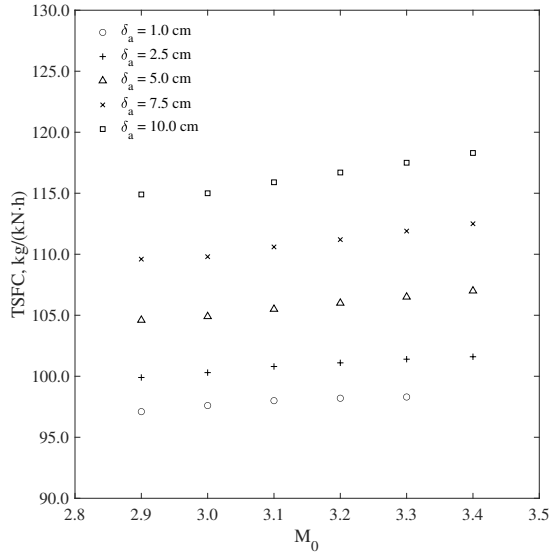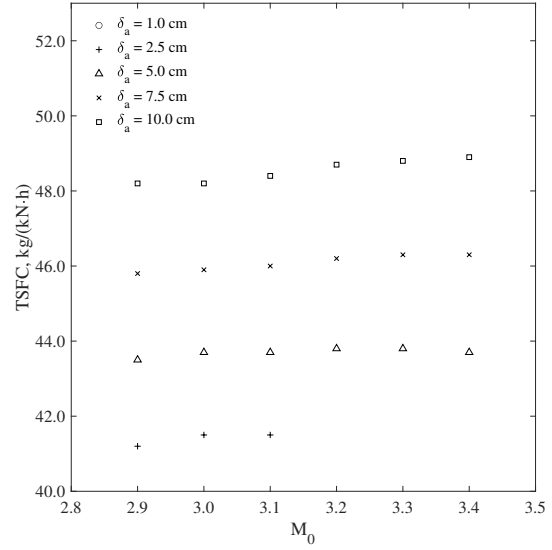
(a) Propane   (b) Hydrogen

Figure 38: STI–2 integrated with parametric RDE performance, TSFC

The thrust-specific fuel consumption for the propane cases was approximately 2.4 times greater than the TSFC of hydrogen cases. Similar to the $(I_{sp})_f$, there was not a large variation in TSFC as Mach number changes.

To reiterate, it was found that the highest performing RDEs were those of the shortest engine length within the parametric sweep; generally, $l = 15$ cm. Also, the performance metric of torque was abandoned as minimizing τ worked against the other three performance metrics. Table 18 shows the cases of highest performance for each metric.

Table 18: High performance cases for STI–2 integrated with RDE

Case	Fuel	M_∞	δ_a, cm	F_z, kN	τ, N·m	$(I_{sp})_f$, s	TSFC, kg/(kN·h)
Maximum F_z	propane	3.4	10.0	24.3	178	3 110	118
Maximum $(I_{sp})_f$	hydrogen	2.9	2.5	4.64	101	9 013	41.2
Minimum TSFC	hydrogen	2.9	2.5	4.64	101	9 013	41.2

Note, the maximum $(I_{sp})_f$ and minimum TSFC cases occurred for the same annulus length and thickness. Unless, one needed to prioritize thrust it would seem to reason to select a hydrogen-fueled RDE of $l = 15$ cm, $\delta_a = 2.5$ cm. However, reviewing Figures 35–38 shows

that solutions failed to converge throughout the entire range of Mach numbers for $\delta_a = 2.5$ cm. If one increases the annular thickness to 5 cm, the resultant torque of the RDE sharply increases. Let δ_a be increased to 10 cm. At this engine configuration, the $(I_{sp})_f$ and TSFC were comparatively worse than the maximum $(I_{sp})_f$/minimum TSFC case, but the $(I_{sp})_f$ and TSFC were still much better than the maximum F_z case. Therefore, for STI–2, an RDE with an annulus length of 15 cm and width of 10 cm was selected as the best performing integrated pair across the Mach range of 2.9 to 3.4.

4.5   Conclusion

Table 19 collects the STI/RDE performance from §4.4.1 and §4.4.2.

Table 19: Summary of STI/RDE Performance

M_∞	RDE for STI–1			
	F_z, kN	τ, N·m	$(I_{sp})_f$, s	TSFC, kg/(kN·h)
2.9	10.3	74.1	7575	48.6
3.0	14.8	106	7619	48.3
3.1	16.1	122	7586	48.5
3.2	17.8	141	7552	48.7
3.3	19.9	166	7535	48.9
3.4	22.5	197	7516	49.0
M_0	RDE for STI–2			
	F_z, kN	τ, N·m	$(I_{sp})_f$, s	TSFC, kg/(kN·h)
2.9	11.6	87.8	7638	48.2
3.0	15.5	111	7631	48.2
3.1	17.1	129	7601	48.4
3.2	19.0	150	7567	48.7
3.3	21.2	177	7547	48.8
3.4	23.9	208	7526	48.9

An RDE configuration with an annulus length of $l = 15$ cm and width of $\delta_a = 10$ cm was selected for both STI types. Both STIs used hydrogen. Therefore, the differences in performance in Table 19 were due to the differences in the STI. Across the entire Mach range, STI–2 outperformed STI–1 by a small margin with exception to resultant torque on the RDE

control volume. For resultant torque, STI–1 resulted in a slightly smaller resultant torque. Although the differences in performance for the integrated systems were small, considering the conclusions presented in §3.7 the better performing integrated STI/RDE system is the system using STI–2.

Mizener et al. reduced the resultant torque on the control volume by lengthening the annulus. Their chosen annulus dimensions were $l = 30$ cm and $\delta_a = 5.0$ cm [58]. The performance results for the integrated STI/RDE for that annulus size can be seen in Table 20.

Table 20: Comparison of integrated RDE, $l = 30$ cm, $\delta_a = 5.0$ cm, at $M_\infty = 3.0$

Inlet	Fuel	F_z, kN	τ, N·m	$(I_{sp})_f$, s	TSFC, kg/(kN·h)
Mizener et al. Model #2	hydrogen	8.5	19	6 615	55.5
Mizener et al. Model #2	propane	8.6	9	2 772	132.3
STI–1	hydrogen	8.0	18.2	6 592	55.7
STI–1	propane	8.3	8.9	2 765	132.7
STI–2	hydrogen	8.4	18.9	6 604	55.6
STI–2	propane	8.6	9.3	2 770	132.5

The integrated STI/RDE systems performed comparably with Mizener et al.'s models with exception to the systems integrated with STI–1. Comparing the performance of the integrated systems in Table 20, for both fuels, the systems using STI–1 yielded slightly lower engine performance. Comparing Mizener et al.'s results to the STI/RDE results presented in Table 19, the systems integrated with an STI outperformed Mizener et al.'s in terms of thrust, fuel-based specific impulse, and thrust-specific fuel consumption. Note, the resultant torque on the control volume for the integrated STI/RDE system was greater than that of Mizener et al.'s results by over a factor of 5.

5 Conclusions and Future Work

5.1 STI Design

Two streamline-traced inlets were designed for flight at an altitude of 18 km and Mach number of 3. Both inlets consisted of an initial deflection wedge, an isentropic compression surface, and an internal compression system. Their difference was the choice of internal compression system: STI–1 used a single-sided compression system, and STI–2 used a symmetrical compression system. The geometry of the isentropic compression surface was defined by a streamline tracing the flow through a truncated, two-dimensional, isentropic compression flowfield. The method of characteristics was used to resolve the flow properties throughout the flowfield. The performance sensitivity of the STIs was determined by a parametric sweep varying the initial deflection angle and Mach number at the entrance of the internal compression system. Both STI designs were optimized for the combination of total pressure recovery and volumetric efficiency by gradient-ascent optimization.

The commercial software ANSYS Fluent was used to analyse the flowfields and assess the STI performance. For a Mach number range of 2.9 to 3.4, the total pressure and Mach number were determined at the inlet exit plane. These values were used in the integration study with the RDE model. It was shown that STI–2 exhibited greater performance across the entire Mach range. STI–2 had a marginally greater volumetric efficiency and was marginally shorter than STI–1. For the total pressure recovery, STI–2 was greater across the entire Mach range and exceeded STI–1 by over 5 percent for the design cases. At subcritical conditions, STI–1 failed to start and a normal shock stood in front of the internal compression system.

The STI performance results were compared with the waverider forebody results in Mizener et al. [58]. At $M_\infty = 3$, the total pressure recovery of STI–1 exceeded Mizener et al.'s Model #1 by approximately 0.13, and STI–2 exceeded Mizener et al.'s Model #2 by approximately 0.02. The volumetric efficiency was only reported for Model #2 in [58]. The volumetric efficiency of STI–2 exceeded Mizener et al.'s Model #2 by 4.6–6.5 percent. It was

shown that the performance of STI–2 exceeded that of STI–1 and the waverider forebodies in Mizener et al. [58]. From the analyses, it can be concluded that the performance of a mixed compression inlet utilizing symmetrical internal compression exceeded single-sided internal compression; this conclusion is corroborated by Mizener et al. [58]. Additionally, at the design Mach number, STIs appeared to exhibit similar total pressure recovery performance when compared to osculating flowfield-based waverider forebody [58], but the STI was able to provide greater volumetric efficiency.

5.2   STI/RDE Integration

The total pressure, total temperature, and Mach number at the STI exit plane were used as the incoming conditions for the RDE. Performance metrics of the RDE were chosen to be the thrust, torque, fuel-based fuel consumption, and thrust-specific fuel consumption. The performance sensitivity of the RDE due to annulus length and annulus width was determined for hydrogen and propane, respectively. From the parametric sweep, it was found that the best RDE performance was for a short and thick annulus with exception to torque. The best performance for minimal torque occurred for long RDE annuli. For both STIs, the maximum fuel-based specific impulse and minimum thrust-specific fuel consumption occurred for the same RDE annulus configuration using hydrogen as fuel.

Across the range of Mach numbers for the STIs, the best integrated STI/RDE performance for thrust, fuel-based specific impulse, and thrust-specific fuel consumption occurred at on-design conditions. As Mach number increased, thrust and torque increased. The fuel-based specific impulse and thrust-specific fuel consumption were found to be insensitive to Mach number. When compared to the reported values for the optimum configuration in Mizener et al. [58], the thrust of the hydrogen-fueled STI–2/RDE system was greater by 82 percent, the fuel-based specific impulse was greater by 15 percent, the thrust-specific fuel consumption was lesser by 13 percent, and the torque was greater by 580 percent. The integrated STI/RDE performance was also determined for the optimum annulus configuration

in [58] integrated with STI–1 and STI–2 for hydrogen and propane. The performance of the integrated STI/RDE systems was found to be comparable to that reported in [58].

From the integration studies, it was found that the differences in the integrated system performance was due to the differences in STI designs. This was solely related to the total pressure available at the STI exit plane. Mizener et al. [58] noted a similar conclusion.

5.3 Future Work

This study considered two-dimensional STI configurations. Future work could include developing an axisymmetric STI using a similar methodology presented in the inlet design section. Additionally, other features to aid operation in a wider range of Mach number should be considered, which may include variable geometry, inlet flow bleed, consideration of spillage for the on-design case, bypass flows, as well as boundary layer corrections.

Optimization of the RDE performance including the minimization of the resultant torque could be performed in the future. Geometry and equipment immediately downstream of the RDE may be considered in attempt to deswirl the flow such as guide/turning vanes. This could lead to a better choice of RDE configuration for applications in the future.

References

[1] Henry, J.R., and Anderson, G.Y., "Design Considerations for the Airframe-Integrated Scramjet," NASA TM X-2895, 1973.

[2] Kumar, A., "Numerical Simulation of Scramjet Inlet Flow Fields," NASA Technical Paper 2517, 1986.

[3] Blankson, I.M., "Air-Breathing Hypersonic Cruise: Prospects for Mach 4–7 Waverider Aircraft," *Proceedings of the ASME 1992 International Gas Turbine and Aeroengine Congress and Exposition*, Cologne, Germany, 1992.

[4] Barkmeyer, D.E.F, Starkey, R.P., and Lewis, M.J., "Inverse Waverider Design for Inward Turning Inlets," AIAA Paper 2005-3915, 2005.

[5] Matthews, A.J. and Jones, T.V., "Design and Test of a Modular Waverider Hypersonic Intake," *Journal of Propulsion and Power*, vol. 22, no. 4, pp. 913–920, 2006.

[6] You, Y. and Liang, D., "Design Concept of Three-Dimensional Section Controllable Internal Waverider Hypersonic Inlet," *Science in China Series E: Technological Sciences*, vol. 52, pp. 2017–2028, 2009.

[7] Hawkins, J.E., "YF-16 Inlet Design and Performance," *AIAA Journal of Aircraft*, vol. 13, no. 6, pp. 436–441, 1976.

[8] Imfeld, W.F., "Development Program for the F-15 Inlet," *AIAA Journal of Aircraft*, vol. 13, no. 4, pp. 286–291, 1976.

[9] Porcher, C.E., and Thebiay, F.J., "Development of the Variable Geometry Inlet for the B-58 Airplane," SAE TP 620327, 1962.

[10] Slater, J.W., "Design and Analysis Tool for External-Compression Supersonic Inlets," NASA TM 2012-217660, 2012.

[11] Nicholls, J.A., Dabora, E.K., and Gealer, R.L., "Studies in Connection with Stabilized Gaseous Detonation Waves," *7th Symposium (International) on Combustion and Detonation*, Butterworths, London, pp. 766–772, 1958.

[12] Wolański, P., "Detonative Engines," *Journal of KONES Powertrain and Transport*, vol. 18, no. 3, pp. 515–521, 2011.

[13] Wolański, P., "Detonative Propulsion," *Proceedings of the Combustion Institute*, vol. 34, no. 1, 2012.

[14] Seddon, J., and Goldsmith, E.L., *Intake Aerodynamics*, Collins, London, 1985.

[15] Evvard, J.C., and Maslen, S.H., "Three-Dimensional Supersonic Nozzles and Inlets of Arbitrary Exit Cross Section," NACA Technical Note 2688, 1952.

[16] Slater, J.W., "Methodology for the Design of Streamline-Traced External-Compression Supersonic Inlets," AIAA Paper 2014-3593, 2014.

[17] Otto, S., Trefny, C.J., and Slater, J.W., "Inward-Turning Streamline-Traced Inlet Design Method for Low-Boom, Low-Drag Applications," *Journal of Propulsion and Power*, vol. 32, no. 5, pp. 1178–1189, 2016.

[18] Slater, J.W., "Design Factors for Two-Dimensional, External-Compression Supersonic Inlets," AIAA Paper 2020-2090, 2020.

[19] Mölder, S., and Szpiro, E.J., "Busemann Inlet for Hypersonic Speeds," *Journal of Spacecraft and Rockets*, vol. 3, no. 8, pp. 1303–1304, 1966.

[20] Van Wie, D., and Mölder, S., "Applications of Busemann Inlet Designs for Flight at Hypersonic Speeds," AIAA Paper 92-1210, 1992.

[21] Billig, F., Baurle, R., Tam, C.-J., and Wornom, S., "Design and Analysis of Streamline Traced Hypersonic Inlets," AIAA Paper 99-4974, 1999.

[22] Billig, F.S. and Kothari, A.P., "Streamline Tracing: Technique for Designing Hypersonic Vehicles," *Journal of Propulsion and Power*, vol. 16, no. 3, pp. 465–471, 2000.

[23] Chao, T., Ni, L., Guanghong, G., and Zeya, S., "A Parameterized Geometry Design Method for Inward Turning Inlet Compatible Waverider," *Chinese Journal of Aeronautics*, vol. 26, no. 5, pp. 1135–1146, 2013.

[24] Wang, X.-D., Wang, J.-F., and Lyu, Z.,-J., "A New Integration Method Based on the Coupling of Multistage Osculating Cones Waverider and Busemann Inlet for Hypersonic Airbreathing Vehicles," *Acta Astronautica*, vol. 126, pp. 424–438, 2016.

[25] Zuo, F., Huang, G., and Xia, C., "Investigation of Internal-Waverider-Inlet Flow Pattern Integrated with Variable-Geometry for TBCC," *Aerospace Science and Technology*, vol. 59, pp. 69–77, 2016.

[26] Oswatitsch, K., "Pressure Recovery for Missiles with Reaction Propulsion at High Supersonic Speeds," NACA TM-1140, 1947.

[27] Liepmann, H.W., and Roshko, A., *Elements of Gasdynamics*, John Wiley & Sons, New York, 1957.

[28] Anderson, J.D., Jr., *Modern Compressible Flow*, McGraw Hill, New York, 2003.

[29] Humphrey, H.A., "An Internal-Combustion Pump, and Other Applications of a New Principle," *Proceedings of the Institution of Mechanical Engineers*, vol. 77, no. 1, pp. 1075-1200, 1909.

[30] Zeldovich, Y.B., "On the Theory of the Propagation of Detonation in Gaseous Systems," NACA TM-1261, 1950.

[31] Shaw, I.J., Kildar, J.A.C., Evans, M.J., Chinnici, A., Sparks, C.A.M., Rubaiyat, S.N.H., Chin, R.C., and Medwell, P.R., "A Theoretical Review of Rotating Deto-

nation Engines," *Direct Numerical Simulations—An Introduction and Applications*, IntechOpen, 2019.

[32] Witenberger, E., and Shepherd, J.E., "Thermodynamic Cycle Analysis for Propagating Detonations," *Journal of Propulsion and Power*, vol. 22, no. 3, pp. 694–697, 2006.

[33] Bulat, P.V., and Volkov, K.N., "The History of the Study of Detonation," *International Journal of Environmental & Science Education*, vol. 11, no. 11, pp. 4894–4909, 2016.

[34] Joshi, D.D., "Unsteady Thrust Measurement Techniques for Pulse Detonation Engines," Ph.D. dissertation, University of Texas at Arlington, Arlington, Texas, 2014.

[35] Glassman, I., Yetter, R.A., and Glumac, N.G., *Combustion*, 5th edition, Academic Press, Amsterdam, 2015.

[36] Vutthivithayarak, R., Braun, E.M., and Lu, F.K., "On Thermodynamic Cycles for Detonation Engines," *28th International Symposium on Shock Waves*, edited by Kontis, K., Paper 2011-2645, University of Manchester, Manchester, England, U.K., 2011.

[37] Lu, F.K., and Braun, E.M., "Rotating Detonation Wave Propulsion: Experimental Challenges, Modeling, and Engine Concepts," *Journal of Propulsion and Power*, vol. 30, no. 5, pp. 1125–1142, 2014.

[38] Kailasanath, K., "Review of Propulsion Applications of Detonation Waves," *AIAA Journal*, vol. 38, no. 9, pp. 1698–1798, 2000.

[39] Sargent, W.H. and Gross, R.A., "Detonation Wave Hypersonic Ramjet," *American Rocket Society Journal*, vol. 30, no. 6, pp. 543–549, 1960.

[40] Morrison, R.B., "Oblique Detonation Wave Ramjet," NASA CR-159192, 1980.

[41] Jiang, Z., Zhang, Z., Liu, Y., Wang, C., and Luo, C., "Criteria for Hypersonic Airbreathing Propulsion and its Experimental Verification," *Chinese Journal of Aeronautics*, vol. 34, no. 3, pp. 94–104, 2021.

[42] Ostrander, M.J., Hyde J.C., Young, M.F., Kissinger, R.D., and Pratt, D.T., "Standing Oblique Detonation Wave Engine Performance," AIAA Paper 87-2002, 1987.

[43] Pratt, D.T., Humphrey, J.W., and Glenn, D.E., "Morphology of Standing Oblique Detonation Waves," *Journal of Propulsion and Power*, vol. 7, no. 5, pp. 837–845, 1991.

[44] Nicholls, J.A., Cullen, R.E., and Ragland, K.W., "Feasibility Studies of a Rotating Detonation Wave Rocket Motor," *Journal of Spacecraft and Rockets*, vol. 3, no. 6, pp. 893–898, 1966.

[45] Bykovskii, F.A., Zhdan, S.A., and Verdernikov, E.F., "Continuous Spin Detonations," *Journal of Propulsion and Power*, vol. 22, no. 6, pp. 1204–1216, 2006.

[46] Kailasanath, K., "The Rotating Detonation-Wave Engine Concept: A Brief Status Report," AIAA Paper 2011-0580, 2011.

[47] Braun, E.M., "New Detonation Concepts for Propulsion and Power Generation," Ph.D. dissertation, University of Texas at Arlington, Arlington, Texas, 2012.

[48] Kailasanath, K., "Recent Developments in the Research on Rotating-Detonation-Wave Engine," AIAA Paper 2017-0784, 2017.

[49] Fievisohn, R.T. and Yu, K.H., "Steady-State Analysis of Rotating Detonation Engine Flowfields with the Method of Characteristics," *Journal of Propulsion and Power*, vol. 33, no. 1, 2017.

[50] Mizener, A.R. and Lu, F.K., "Low-Order Parametric Analysis of a Rotating Detonation Engine in Rocket Mode," *Journal of Propulsion and Power*, vol. 33, no. 6, 2017.

[51] Mizener, A.R., "Performance Modeling and Experimental Investigations of Rotating Detonation Engines," Ph.D. dissertation, University of Texas at Arlington, Arlington, Texas, 2018.

[52] Braun, E.M., Lu, F.K., Wilson, D.R., and Camberos, J.A., "Airbreathing Rotating Detonation Wave Engine Cycle Analysis," *Aerospace Science and Technology*, vol. 27, no. 1, pp. 201–208, 2013.

[53] Welsh, D.J., King, P.I., DeBarmore, N.D., Schauer, F.R., and Hoke, J.L., "RDE Integration with T63 Turboshaft Engine Components," AIAA Paper 2014-1316, 2014.

[54] Paxson, D.E. and Naples, A., "Numerical and Analytical Assessment of a Coupled Rotating Detonation Engine and Turbine Experiment," AIAA Paper 2017-1746, 2017.

[55] Rankin, B.A., Fotia, M.L., Naples, A.G., Stevens, C.A., Hoke, J.L., Kaemming, T.A., Theuerkauf, S.W., and Schauer, F.R., "Overview of Performance, Application, and Analysis of Rotating Detonation Engine Technologies," *Journal of Propulsion and Power*, vol. 33, no. 1, pp. 131–143, 2017.

[56] Frolov, S.M., Zvegintsev, V.I., Ivanov, V.S., Aksenov, V.S., Shamshin, I.O., Vnuchkov, D.A., Nalivaichenko, D.G., Berlin, A.A., and Fomin, V.M., "Demonstrator of Continuous-Detonation Air-Breathing Ramjet: Wind Tunnel Data," *Physical Chemistry*, vol. 474, no. 1, pp. 75–79, 2017.

[57] Frolov, S.M., Zvegintsev, V.I., Ivanov, V.S., Aksenov, V.S., Shamshin, I.O., Vnuchkov, D.A., Nalivaichenko, D.G., Berlin, A.A., and Fomin, V.M., "Continuous Detonation Combustion of Hydrogen: Results of Wind Tunnel Experiments," *Combustion, Explosion, and Shock Waves*, vol. 54, no. 3, pp. 357–363, 2018.

[58] Mizener, A.R., Lu, F.K., and Rodi, P.E., "Performance Sensitivities of Rotating Detonation Engines Installed onto Waverider Forebodies," *Journal of Propulsion and Power*, vol. 35, no. 2, 2019.

[59] Bedick, C., Sisler, A., Ferguson, D., Strakey, P. Nix, A., and Billips, D., "Development of a Lab-Scale Experimental Testing Platform for Rotating Detonation Engine Inlets," AIAA Paper 2017–0785, 2017.

[60] Hishida, M., Fukiwara, T., and Wolanski, P., "Fundamentals of Rotating Detonations," *Shock Waves*, vol. 19, pp. 1–10, 2009.

[61] Perkins, H.D. and Paxson, D.E., "Summary of Pressure Gain Combustion Research at NASA," NASA/TM–2018-219874, 2018.

[62] Paxson, D.E. and Perkins, H.D., "Thermal Load Considerations for Detonative Combustion-Based Gas Turbine Engines," AIAA Paper 2004-3396, 2004.

[63] Naples, A., Fotia, M., Scott, T., Hoke, J., and Schauer, F., "Design and Testing of a Rotating Detonation Engine for Open-Loop Gas Turbine Integration," *Proceedings of the 25th International Colloquium on the Dynamics of Explosions and Reactive Systems*, Paper 019, 2015.

[64] Thompson, P.A., *Compressible-Fluid Dynamics*, McGraw–Hill, New York, 1971.

[65] Zucrow, M.J. and Hoffman, J.D., *Gas Dynamics, Volume I*, John Wiley & Sons, New York, 1976.

[66] Zucrow, M.J. and Hoffman, J.D., *Gas Dynamics, Volume II: Multidimensional Flow*, John Wiley & Sons, New York, 1977.

[67] Wang, Y., Shi, W., Wang, X., Zhang, J., Gao, J., Tang, J., Chang, J., and Bao, W., "Aerodynamic Performance Enhancement of a Variable-Geometry Dual-Mode Combustor designed by the Method of Characteristics," *Aerospace Science and Technology*, vol. 108, Paper 106353, 2021.

[68] Hall, I.M., "Inversion of the Prandtl–Meyer Relation," *Aeronautical Journal*, vol. 79, no. 777, pp. 417–418, 1975.

[69] McBride, B.J., Gordon, S., and Reno, M.A., "Coefficients for Calculating Thermodynamic and Transport Properties of Individual Species," NASA TM 4513, 1993.

[70] "U.S. Standard Atmosphere, 1976," NASA TM-X-74335, 1976.

[71] O'Brien, T.F. and Colville, J.R., "Analytical Computation of Leading-Edge Truncation Effects on Inviscid Busemann-Inlet Performance," *Journal of Propulsion and Power*, vol. 24, no. 4, pp. 655–661, 2008.

[72] Zhao, Z. and Song, W., "Effect of Truncation on the Performance of Busemann Inlet," *Modern Applied Science*, vol. 3, no. 2, pp. 168–171, 2009.

[73] Utomo, M.A. and Bura, R.O., "Design of Inward-Turning External Compression Supersonic Inlet for Supersonic Transport Aircraft," *International Series on Interdisciplinary Science and Technology*, vol. 2, no. 2, pp. 104–110, 2017.

[74] "Engine, Aircraft, Turbojet and Turbofan, General Specification for," MIL-E-5007D, 1973.

[75] Yang, X.-S., "3—Optimization Algorithms," *Introduction to Algorithms for Data Mining and Machine Learning*, Academic Press, London, pp. 45–65, 2019.

[76] Conti, R.S. and Hertzberg, M., "Thermal Autoignition Temperatures for Hydrogen-Air and Methane-Air Mixtures," *Journal of Fire Sciences*, vol. 6, no. 5, pp. 348–355, 1988.

[77] Bounaceur, R., Glaude, P.-A., Sirjean, B., Fournet, R., Montagne, P., Vierling, M., and Molière, M., "Prediction of Auto-Ignition Temperatures and Delays for Gas Turbines Applications," *Journal of Engineering for Gas Turbines and Power*, vol. 138, no. 2, Paper 021505, 2016.

[78] Kantrowitz, A. and Donaldson, C.duP., "Preliminary Investigation of Supersonic Diffusers," NACA Advance Confidential Report L5D20, 1945.

[79] "Standard Thermodynamic Properties of Chemical Substances," *CRC Handbook of Chemistry and Physics*, edited by D.R. Lide, CRC Press, Boca Raton, Florida, pp. 5-4–5-42, 2005.

[80] Gurvich, L.V., Iorish, V.S., Yungman, V.S., and Dorofeeva, O.V., "Thermodynamic Properties as a Function of Temperatrue," *CRC Handbook of Chemistry and Physics*, edited by D.R. Lide, CRC Press, Boca Raton, Florida, pp. 5-43–5-65, 2005.

[81] Goodwin, D.G., Moffat, H.K., and Speth, R.L., "Cantera: An Object-Oriented Software Toolkit for Chemical Kinetics, Thermodynamics, and Transport Processes," Version 2.4.0, 2017, cantera.org.

[82] "Shock and Detonation Toolbox - Version 2021," California Institute of Technology, Explosion Dynamics Lab, Pasadena, California, https://shepherd.caltech.edu/EDL/PublicResources/sdt/.

[83] Paxson, D.E., "Numerical Analysis of a Rotating Detonation Engine in the Relative Reference Frame," AIAA Paper 2014-0284, 2014.

[84] Nordeen, C.A., Schwer, D., and Corrigan, A., "Area Effects on Rotating Detonation Engine Performance," AIAA Paper 2014-3900, 2014.

[85] Hayashi, A.K., Kimura, Y., Yamada, T., Yamada, E., Kindraki, J., Dzieminska, E., Wolanski, P., Tusboi, N., Tangirala, V.E., and Fuiwara, T., "Sensitivity Analysis of Rotating Detonation Engine with a Detailed Reaction Model," AIAA Paper 2009-0633, 2009.

[86] Schwer, D.A. and Kailasanath, K., "Numerical Investigation of Rotating Detonation engines," AIAA Paper 2010-6880, 2010.

[87] Braun, E.M., Lu, F.K., Wilson, D.R., and Camberos, J.A., "Airbreathing Rotating Detonation Wave Engine Cycle Analysis," AIAA Paper 2010-7039, 2010.

[88] Schwer, D. and Kailasanath, K., "Numerical Investigation of the Physics of Rotating-Detonation-Engines," *Proceedings of the Combustion Institute*, vol. 33, pp. 2195–2202, 2011.

[89] Nordeen, C.A., Schwer, D., Corrigan, A., and Cetegen, B., "Radial Effects on Rotating Detonation Engine Swirl," AIAA Paper 2015-3781, 2015.

[90] Fievisohn, R.T. and Yu, K.H., "Parametric Study of an Ethylene–Air Rotating Detonation Engine Using an Ideal Model," AIAA Paper 2016-1403, 2016.